Photon-Hadron Jet Correlations in d-Au Collisions with $\sqrt{S} = 200$GeV at RHIC

Bing Xia

Submitted in partial fulfillment of the requirements for
Ph.D prospectus
in the School of Arts and Sciences

Department of Physics and Astronomy
Ohio University

October 2010

Abstract

The direct photon probe serves as a golden channel of energy loss of jets at RHIC, especially in nuclear collisions. The two-particle azimuthal correlations between the π^0 and direct photon triggers of $5 < p_T < 15$ GeV and the charged hadron partners of $1 < p_T < 10$ GeV will be measured in PHENIX Run 8 dAu data set. Besides the conventional statistical subtraction method, the first application of isolation cut at RHIC in a high multiplicity environment will be adopted to enhance the direct photon signal. The per-trigger yield will be obtained to investigate the away-side jet properties in the cold nuclear matter environment, such as suppression of the yield or the nuclear kT effect which is an imbalance of out going di-jet momentum which should normally be balanced in simple 2 to 2 scattering. These effects are expected due to interactions of the outgoing jets with the heavy Au nucleus, as they propogate through. Possible modification of the initial state quarks (q) and gluons (g), due to the nuclear structure will also be investigated at forward rapidity, such as gluon saturation phenomena effects. In addition, the difference between gluon/quark jets and up-/down-quark jets already maybe seen in p+p collisions, can be verified and studied in d+Au collisions, which will explore "baseline" nuclear effects of this probe which is important for the use of such information in studying the hot plasma created in Au+Au collisions. Some similar investigations of Au+Au data, may also be attempted if time permits.

Contents

List of Figures

List of Tables

Chapter 1

Introduction and Motivation

The quarks are confined in the hadrons in normal state, and never found in a free and isolated state, which is known as the color confinement phenomena. Theoretical calculation shows that the quarks could be deconfined in a condition of extreme high temperature or density, as shown in Figure 1.1, which exists in the first a few microseconds of the universe. In the laboratory environment, this new state of quark matter, the quark gluon plasma (QGP), could be achieved by the relativistic heavy ion collider (RHIC). Since the commission of RHIC in the beginning of 21st century, various measurements have been conducted in the search of the signature of quark gluon plasma created in heavy ion collisions and to test nuclear theories, including the suppression of the energetic particles, elliptic flows with low viscosity. Meanwhile, these theories, which are be based on quantum chromodynamics (QCD) are also tested by RHIC data through the interaction between the outgoing parton with matter, and the fragmentation process in different scenarios, such propagation through the QGP or through normal nuclear matter.

Medium Effects

The yields of hadrons (bound states of quarks) with high outgoing momentum transverse to the incoming beams (p_T) are discovered to be largely suppressed in central Au+Au collisions compared to p+p collisions [2] due to the energy loss of the final state jets in the opaque hot medium, while there sis a small enhancement in the intermediate p_T region in d+Au collisions [3] known as the Cronin effect. The Cronin effect is attributed to the multiple scatterings in the cold nuclear medium, which is absent in p+p collisions. Also, a broadening

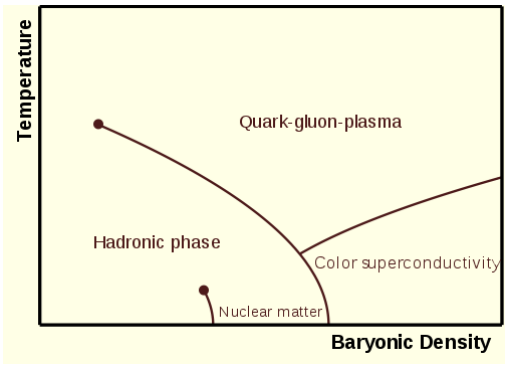

Figure 1.1: QCD Phase Diagram, the low temperature and low density state is the hadron phase, which is common in the nuclear matter, the high temperature and high density state is the quark-gluon plasma, and the low temperature and high density state is the color superconductivity phase [1]

Figure 1.2: The Leading-Order Feynman diagram which contributes to the prompt photon production. From left to right, the s and u channel of quark gluon Compton scattering, the t and u channel of quark anti-quark annihilation [7]

of the dijet distribution in d+Au collisions is reported in [4], which might come from the additional transverse momentum from the multiple scattering in the cold nuclear medium. The d+Au collisions serve as the base line to the A+A (nucleus-nucleus) collisions, in order to differentiate the effect whether coming from the hot medium created in central heavy ion collisions or the cold nuclear medium presented in p+A (proton-nucleus) collisions.

k_T Effect

In the leading order approximation (LO) of QCD scattering, which corresponds to 2 to 2 scattering reactions, such as $q + g \rightarrow q + g$, the transverse momentum of one outgoing *parton* (a generic word for quark or gluon) should be exactly balanced with the other side parton. However, due to the finite size of the nucleons, the initial partons are expected to have a transverse momentum in the order of 300 MeV [5]. The p_T imbalance is further spoiled by the fact that the hard scattered parton could radiate fragmentation photon or bremsstrahlung gluons beyond the LO QCD. Moreover, γ+A and π+A collisions show that $\langle k_T \rangle$ (k_T is defined as the p_T sum of the outgoing partons) is proportional to $A^{1/3}$, which could results from the multiple scattering in the nucleus since $L \sim A^{1/3}$. In p+A collisions, $\langle k_T \rangle$ increases more slowly than $A^{1/3}$ [4]. These effects are collectively called k_T effect. The next-to-leading order (NLO) pQCD calculation is insufficient to describe the magnitude of p_T imbalance measured in the experiments which is about a few GeV in dimuon, diphoton and dijet pairs [6]. The relationship between the k_T effect and the presence of the the nuclear matter, no matter hot or cold nuclear matter, is yet to be discovered by experiments.

Golden Channel

Jets in high energy collisions are useful tools to study the hard scattering partons, which are valuable probes to the hot and dense QGP medium in RHIC. Di-hadron measurements like the π-h azimuthal correlation shows the away-side jet suppression in Au+Au collision [8] [9]. However, the trigger hadron is unable to identify the momentum of the partons, even with a high p_T value, and full jet reconstruction in heavy ion collisions is still in development. Furthermore, the sample of trigger hadrons have high energy, which has a bias on the small energy loss in the medium. The most important bias is the "surface bias", which means the high p_T hadron triggers are more likely coming from the surface of the two-nuclei overlapping zone. In such a case, we are unable to determine for the two high p_T back-to-back hadrons whether they come from the surface with a tangential trajectory or they both originate from the deep inside but with a small number of interactions within the hot medium. The photon is colorless, therefore the interaction cross-section in the nuclear medium is very small compared with the quark and gluon. So the prompt photon is less affected by the QCD medium, see Figure 1.2 for the prompt photon processes. The direct photon (prompt photon + fragmentation photon) sample is unbiased towards any region and the jet suppresion should be an average effect of all path through the medium. Meanwhile, the momentum of the direct photon could serve as an estimation of the momentum of the away-side jet, aside of the k_T effect discussed above. Thus, the direct photon is long viewed as a "golden channel" in heavy ion collision study, though it's much more rare.

Gluon/Quark Jets

Since the quark-gluon Compton scattering is the dominant process for the prompt photon production, whose Feynmann diagrams are shown in Figure 1.2, we expect the away-side jet in the prompt photon events is the fragmentation products from a quark instead of a gluon. Meanwhile the jet in the inclusive sample is a mixture of the gluon and quark jets (in statistical sense). The difference between the gluon and quark jets are expected both in pQCD and non-perturbative QCD since the gluon has doubled color charge compared to the quark. Previous studies showed that the spectrum of the gluon jets are softer (more low energy particles), and the width and multiplicity of the gluon jets are larger than the quark jets. Thus, the direct photon process serves as a good stage to test the difference of quark/gluon jets in the fragmentation function and the parton energy loss in the medium. Furthermore, due to the different valence quark constituents in the proton and neutron, it is possible to observe the difference between an up quark and down quark jet. The Compton scattering cross-section for the up quark is 4 times as large as the down quark (the Compton amplitude could be calculated by the Feynman rule. The quark-gluon interaction vertex term is the same for u and d quark since QCD only depends on the color charge. But for the quark photon QED vertex, there is a quark electromagnetic (EM) charge factor. The amplitude for the up quark is twice as much as down quark, reflecting the charge magnitude difference 2/3 vs 1/3. To get the cross section, we need to square the amplitude. That's where the 4:1 comes from. Then, in a p+p collision, there are twice as many up quarks as down quarks in a proton, so we expect the total ratio between outgoing up and down quark jets is 8:1. This ratio could be diluted by several other uncontrollable factors, such as the creation of quark pairs and parton radiation, which tend to make it less. A previous measurement has been done by [7], and the result is shown in Figure 1.3, which is qualitatively consistent with the above consideration. For d+Au collision, we consider the deuteron nucleus is a combination of loosely bound collection of a proton and a neutron, and the gold nucleus consists of 79 protons and 118 neutrons. If we assume the gluon jet in the initial state of Compton scattering is evenly distributed between the colliding two nuclei, the ratio between the up and down quark jets could be calculated as $\frac{5}{1} \times \frac{197}{394} + \frac{8}{1} \times \frac{79}{394} + \frac{2}{1} \times \frac{118}{394} = 4.7$ in d+Au collisions. In Figure 1.3 from [7], the charge asymmetry in p+p collisions is about 3.5 for high x_E where the up/down quark jet ratio is 8:1. For a naive estimation, I expected we could reach a charge asymmetry around $4.7 \times 3.5/8 \approx 2$, which is still prominent in experiments. As a bonus, if PHENIX could tag the colliding nucleon in the deuteron by considering the ZDC hit in the backward direction, namely the deuteron direction, the expected ratio is $\frac{8}{1} \times \frac{79}{394} + \frac{5}{1} \times \frac{118}{394} = 6.2$ for p-tagged events, and $\frac{5}{1} \times \frac{79}{394} + \frac{2}{1} \times \frac{118}{394} = 4.0$ for n-tagged events. The up and down quark jets are expected to have different properties, such as *the asymmetry betwee the positive and negative charged hadrons* ('cause $q_u = +2/3$, $q_d = -1/3$), or *the ratio between the mesons and baryons* (gluons are more likely to fragmentation into baryons, 'cause $g \sim q\bar{q}$ and has double color charge). This would be the first opportunity to observe such a characteristics difference, at least in RHIC community. This is an extremely important baseline for using such identified jet types in Au+Au studies of energy loss where gluon jets are expected to have larger energy loss through the QGP, again due to larger color charge.

Gluon Saturation

The study of the nuclear modification factor $R_{dAu} \equiv \frac{1}{N_{coll}} \frac{d^2N^{d+Au}/dp_T d\eta}{d^2N^{p+p}_{inel}/dp_T d\eta}$ in d+Au collision at different rapidity and centrality shows a significant forward rapidity suppression, especially in the central collision [10]. The mid-/forward-rapidity and forward-/forward-rapidity two-particle correlation (see details in Section 3.3) is observed to be suppressed for d+Au collision compared with p+p, according to the preliminary result of PHENIX [11]. This effect has been predicted as a signature of the color glass condensate [12]. In this scenario, the short-life fluctuation partons are frozen out due to the time dilation in a fast moving

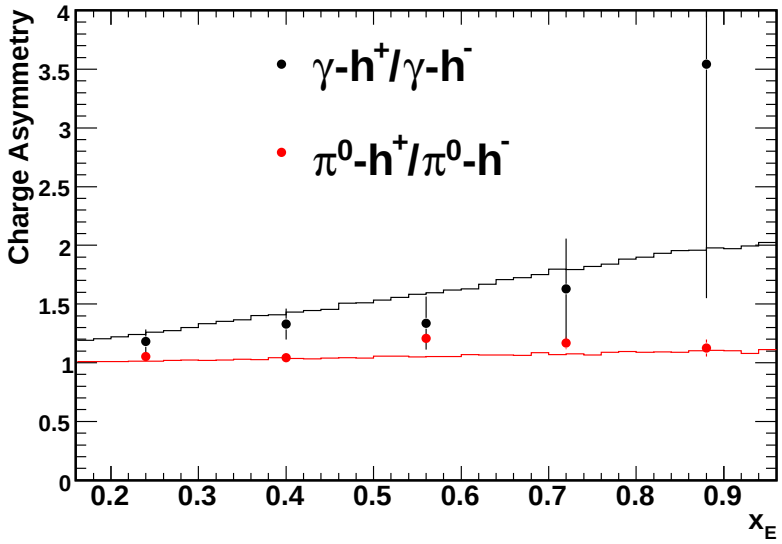

Figure 1.3: Away-side hadron charge asymmetry in p+p collisions [7]: The points in the plot are the experiment data, and the curves are the theoretical calculation. Here, $x_E \equiv -\frac{\vec{p}_T^t \cdot \vec{p}_T^a}{|\vec{p}_T^t|^2}$.

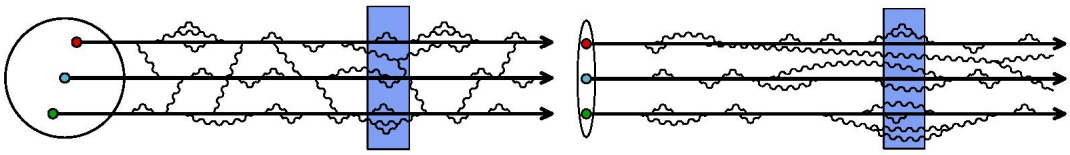

Figure 1.4: Left: a rest nucleon, the parton fluctuation is complicated non-perturbative and short lived. Right: a high energy nucleon, the thickness is compressed due to the length contraction, the short-lived parton fluctuation becomes a static source of parton due to the time dilation.

nucleons, and exist as a large static source of low momentum/energy partons, see Figure 1.4. The gluon density at the small momentum fraction x is the result from the balance of gluon recombination (reducing the number) and gluon splitting (increasing the number), and peaks about a characteristic momentum $Q_S \sim \frac{A^{1/3}}{x^\lambda}$, namely the saturation momentum (here λ is 0.3 determined from data in [11]). Such an effect is called gluon saturation, because below this momentum scale, no more gluons can be created due to the dominance of the recombination. It is predicted that the gluon saturation gets prominent when the jet's p_T is close to Q_s, which is about 1-2 GeV in RHIC and increases with nuclear size as the formula indicates. Therefore, the large nucleus and small x, which is equivalent to the forward region, are favored to test the gluon saturation phenomena. Though, some other theories could explain such a suppression in d+Au collisions, such as the nuclear shadowing. To distinguish these models, the forward azimuthal correlation is suggested to be utilized [13]. Benefitted from the newly installed Muon Piston Calorimeter (MPC) detector located in the forward/backward regions, PHENIX are capable to analyse the two-particle correlation in the forward/backward regions which are separated from the mid-rapidity central arm.

In summary, due to the large multiplicity in heavy ion collision environment, two-particle azimuthal correlations are often used instead of full jet reconstruction. The direct photon trigger could help to remove the "surface bias" in the study and get more insight on the final state medium effect (cold vs hot), k_T

effect(p_T imbalance), jet characteristics (gluon vs quark, up vs down), and the color glass condensate (gluon saturation or not).

Chapter 2

Experimental Apparatus

2.1 RHIC

The Relativistic Heavy Ion Collider(RHIC), as shown in Figure 2.1, is a dedicated heavy ion collider at Brookhaven National Laboratory(BNL) in Upton, New York, USA. RHIC began its physical operation from the year of 2000 with highest energy $\sqrt{S_{NN}}$ = 200GeV for heavy ions and 500GeV for protons. RHIC is capable to collide a variety of beam species, including protons, copper gold and uranium nuclei, in a wide span of energy ranging from a few GeV to its highest energy level. RHIC has its own advantage to collide polarized protons for studying the spin structure of particles. Two small experiments BRAHMS and PHOBOS have finished their operation, and the other two experiments at RHIC, namely PHENIX and STAR are still in operation.

2.2 PHENIX

PHENIX, the Pioneering High Energy Nuclear Interaction eXperiment, shown in Figure 2.2, is a research experiment at RHIC to study the energetic collisions between heavy ions and protons, with the mission of discovery and examination of the new state of matter, namely quark-gluon plasma, as well as the exploration in the spin structure of protons. PHENIX is designed to optimize the capability to detect the rare process

Figure 2.1: A birdview of RHIC with the beam line indicated

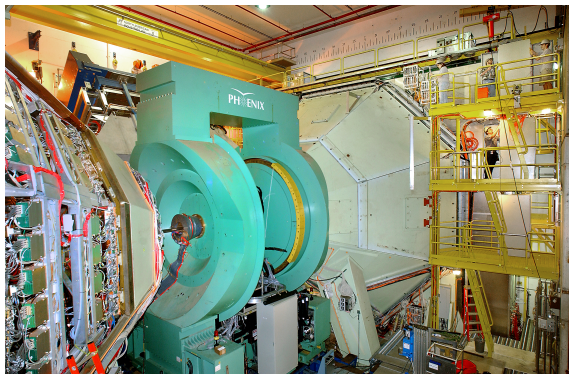

Figure 2.2: A photo of PHENIX detector

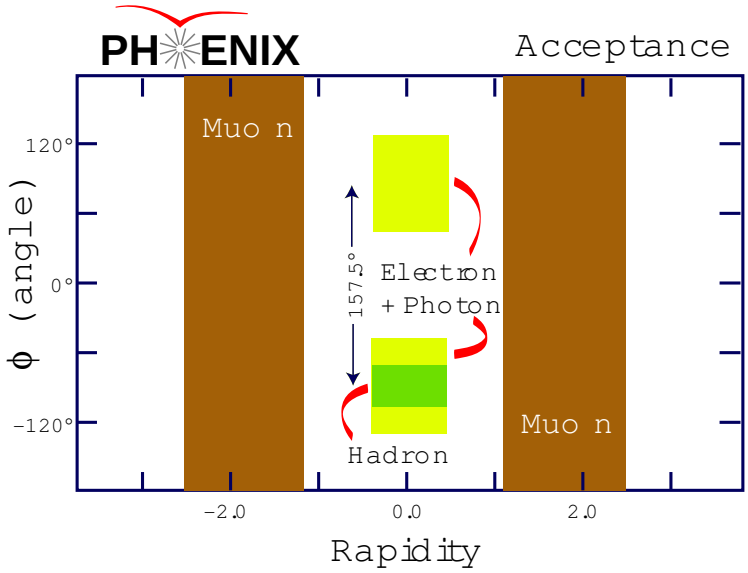

Figure 2.3: PHENIX acceptance plot, ϕ is the azimuthal angle around the beam line, rapidity is along the beam line

with better resolution and momentum range for penetrating probes, such as leptonic(including electrons and muons) and photonic channels. STAR has larger acceptance coverage benefited from their barrel Time Projection Chamber(TPC). Two different detector configurations in STAR and PHENIX experiment could provide both teams their own advantages and the cross-check of their results from different techniques. This complementary setup of experiments is beneficial to the whole physics community. The future installation of new Silicon Vertex Detector(VTX) in Run11 will provide a full azimuthal coverage, and make PHENIX as capable as STAR in the acceptance range. The current PHENIX acceptance coverage is shown in Figure 2.3.

PHENIX is a combination of different particle detectors, which are on four spectrometer arms. The variety of PHENIX detectors provides more measurements and cross-checks for the analysis. The north-south spectrometer arms are along the beam line at the forward and backward rapidity region, with $1.15 < \eta < 2.44$ or $-2.25 < \eta < -1.15$. These two muon arms are designed specifically for muon identification and track reconstruction. The east-west spectrometer arms are on the central rapidity region, on the side of the beam line. The two central arms cover $-0.35 < \eta < 0.35$ in the rapidity and 180° in azimuthal angel. The primary goals of the central arms include photon/electron reconstruction, charged particle tracking, particle identification. The detector configuration of PHENIX Run08 is shown in Figure 2.4.

2.2.1 Event Trigger and Characterization

The inner detectors consists of Beam-Beam Counters(BBCs), Zero Degree Calorimeters(ZDCs) and Reaction Plane Detector(RxNP), which are responsible for the event triggering and characterization, such as determination of the event location, centrality and the reaction plane.

Beam-Beam Counters

The BBC detectors, shown in Figure. 2.5, are placed around the beam pipe at ±144cm from the geometry center of PHENIX detector covering $3.1 < \eta < 3.9$ over full azimuth. The detector consists of a set of

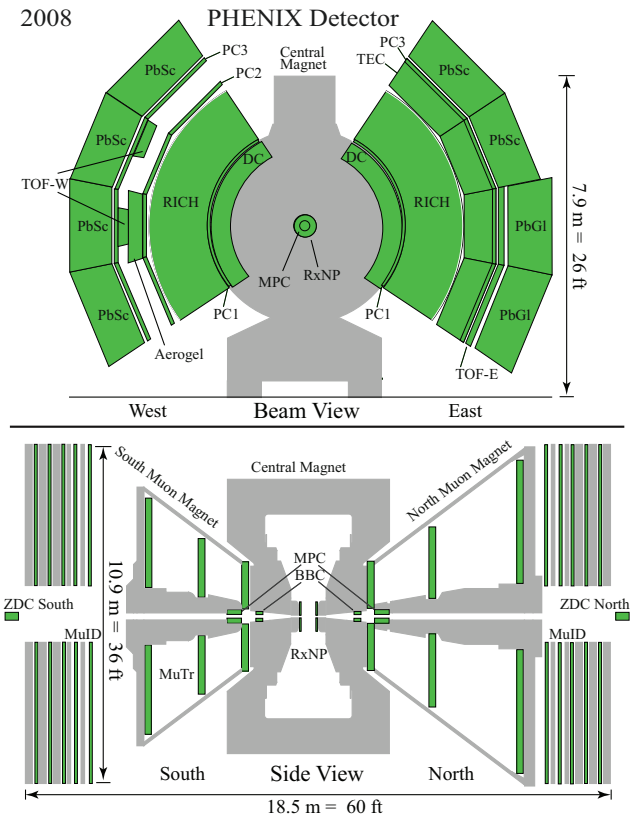

Figure 2.4: PHENIX detector configuration for Run8, top: beam veiw, bottom: side view

64 photonmultiplier tubes(PMT) which measure the Cherenkov light from the charged particles passing through the quartz radiators in front of each PMT. The most important feature of BBC is the excellent timing resolution, about 54 ± 4 ps for each element. The collision time $T0$ is determined by the average arrival time of the leading charged particles into the South and North BBCs. This time is used by the timing synchronization, such as for the TOF detectors of PHENIX to identify hadrons. The collision location, namely Z-vertex, is determined by the difference of the time from the two BBCs with resolution about 1cm, which is part of the Local Level 1 trigger which rejects the collision with Z-vertex outside of the center interaction region(>30cm). The collision vertex is also used as the origin point for tracking subsystems. The resolution gets worse for lower centrality, smaller size of beam species and lower beam energy.

Zero Degree Calorimeters

The ZDC detectors, shown in Figure 2.6, are a pair of hadronic calorimeters located at 18 meters away from the center of PHENIX along the beam pipe, covering $\theta < 2mrad$ ($6\eta > 6$). They are positioned behind the dipole bending magnets such that the charged beam remnants are swept away from their path by the magnetic field. ZDCs are able to catch the spectator neutron remnants with the trajectory very close to the beam line. ZDCs are designed to completely contain the hadronic showers of the spectator neutrons.

The Centrality Definition

PHENIX uses the concept of centrality to characterize the geometric quantity, "impact parameter" b, such that the centrality refers to the percentiles of the total nuclear interaction cross section (7.2 b). The centrality

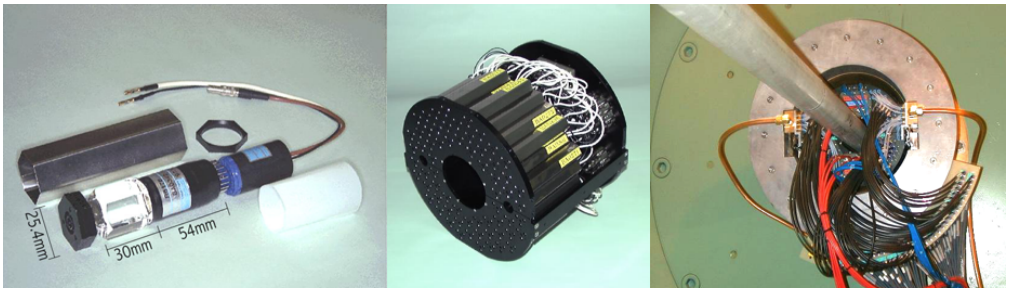

Figure 2.5: BBC detector construction: An individual BBC PMT and quartz radiator (left). A BBC bundle as constructed from 64 PMT and radiators (center). A BBC as installed around the beam pipe behind the central magnet (right).

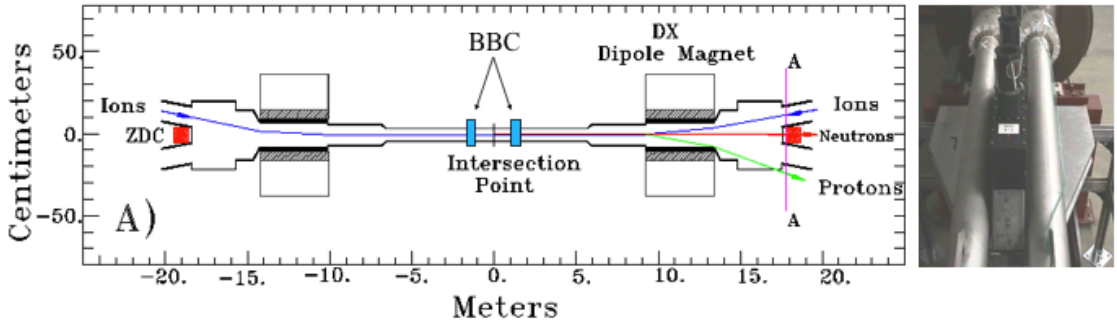

Figure 2.6: Placement of the ZDC beyond the forward dipole magnets(left). A ZDC as installed between the RHIC blue and yellow beam pipes(right).

class could be determined from the experimental observables, like the multiplicity and energy deposition. Using the Glauber model, the impact parameter b and some other collision quantities could be determined for each centrality class. For example, we can measure the charged particle multiplicity dN_{ch}/dN_{evt} in the mid-rapidity $|\eta| < 1$. And the distribution of $d\sigma/dN_{ch}$ is related to dN_{evt}/dN_{ch} by the relation of $N_{evt} = \sigma \int Ldt$. As shown in Figure 2.7, the centrality class is defined by the fraction of the total cross section in a specific bin.

The quantity N_{part} mentioned in Figure 2.7 is a concept of the Glauber model. In the Glauber model, the two colliding nuclei are treated as two collections of incoming nucleons. The nucleus-nucleus collision is deemed as a superposition of multiple nucleon-nucleon collisions. The Glauber model is often calculated by a Monte Carlo simulation. The two nuclei are modeled by the computer as two bunches of independent nucleons distributed as some probability distribution function, which travel in straight lines in 3 dimensional space. A random impact parameter b is picked up with a probability according to $d\sigma/db = 2\pi b$. Each N-N collision is independent of other nucleons or any N-N collisions before, and depends only on the distance d between two participating nucleons. If $d < \sqrt{\sigma_{inel}^{NN}/\pi}$, a collision is set to happen bwtween the two nucleons. There might be some other complicated considerations envolved. In this way, the number of participating nucleons N_{part} and the number of binary nucleon-nucleon collisions N_{coll} are clearly obtained. After many simulations, the average number $\langle N_{part} \rangle$, $\langle N_{coll} \rangle$ and other quantities for some specific impact parameter b, which in turn is related to the centrality, could be determined.

The underlying assumption here is that the impact parameter is monotonically related to the particle multiplicity both at the mid-rapidity and the forward-rapidity regions, or other experimental used observables,

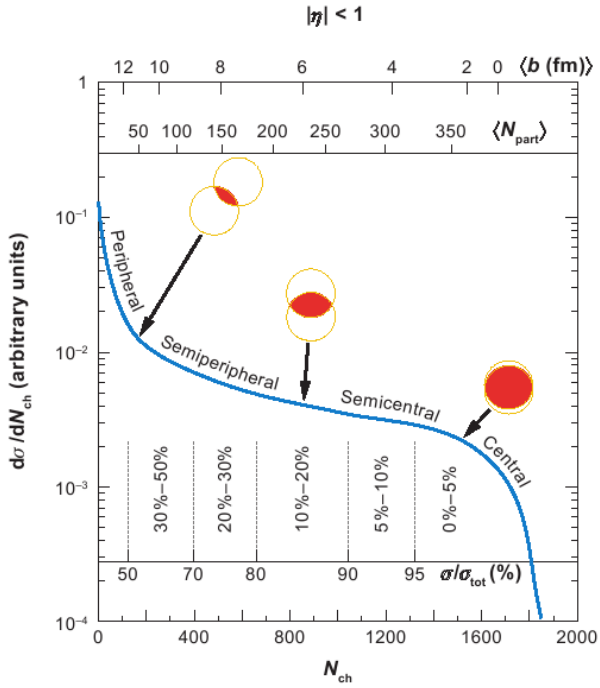

Figure 2.7: Simple example of the definition of the centrality class by the experiment observable, namely the charged particle multiplicity in mid-rapidity N_{ch} [14]. Also, the impact parameter b and the number of participating nucleons N_{part} calculated from the Glauber model are shown in the top of the figure.

to make a one-one mapping between the impact parameter and the class centrality(or say, the experimental observables). If there is no such a monotonical relation, the centrality class obtained in the experiment is irrelevant to the impact parameter b, and can not be used to determine N_{part},N_{coll} by the Glauber model. In the case of large impact parameter or peripheral events, we expect a small particle multiplicity in the mid-rapidity and a larger number of spectator nucleons in the forward-rapidity. On the contrary, we expect a large particle multipliciy in the mid-rapidity and a small number of spectator nucleons in the forward-rapdity for the central events with small impact parameter.

PHENIX adopts a "clock" method to determine the centrality class by the charge collected in BBCs and the energy deposited in ZDCs. The former quantity is determined by the participating nucleons, while the later are determined by the number of neutrons coming from the colliding nuclei. Fiure 2.8 shows the determination of the centrality in PHENIX by BBCs and ZDCs. The response of ZDC is quite interesting. In most central collisions, few spectator neutrons could survive in the collision and reach ZDCs. As the impact parameter increases, more and more spectator neutrons are collected by ZDCs. But, for the most peripheral collisions, though few participating neutrons are envolved in the collisions, most spectator neutrons are still bound with the spectator protons, and are swept out by the magnetic field. Therefore, for the most central collisions, few spectator neutrons could hit ZDCs. The centrality could be determined by the combination of BBCs and ZDCs. As shown in Figure 2.8, the ZDCs are sensitive in the most peripheral collisions, and the BBCs are sensitive in the most central collisions.

Triggers

There are two sets of level-1 (LVL1) triggers available for Run 8 dAu data. One is the Minimum Bias trigger (MB), the other one is the EMCal/RICH Level-1 Trigger (ERT). The LVL1 trigger helps to remove empty beam crossing and uninterested events, and serves an essential part of PHENIX on-line system.

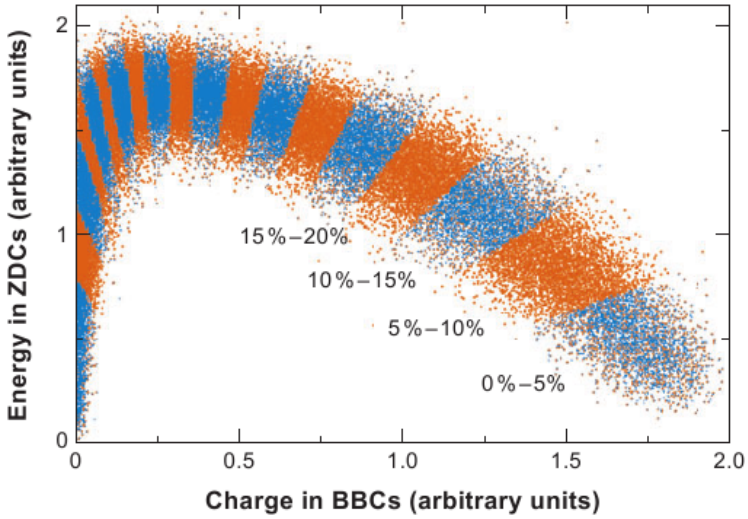

Figure 2.8: The centrality class is determined by the response of BBCs and ZDCs in PHENIX [14].

For Au+Au collisions, the Min Bias trigger requires at least two photomultiplier hits in each BBC for and at least one neutron detected in each ZDC (which helps to remove the background events from beam-gas interaction, but is accompanied by a efficiency lost in the most peripheral collisions due to the ZDCs' poor response in such events.). For p+p, d+Au and Cu+Cu collisions, the Min Bias trigger requires a coincidence between the BBCs with at least one hit in each BBC detector.

Besides the Min Bias trigger, PHENIX utilizes the ERT trigger, which is triggered by the events with high pT photons or electrons. The EMCal and RICH subsystems are used in this Level 1 trigger. In the EMCal part of the ERT trigger, an energy threshhold is required for an overlapping tile of 4x4 EMCal towers in coincidence with the BBC trigger. There are 4 variants, namely 4x4a, 4x4b, 4x4c with different energy thresholds, and 2x2 with an energy thresholds on a tile of 2x2 EMCal towers. This requirement makes sure that there is at least one high pT photon or electron hit in EMCal. In the RICH part of the ERT trigger, a threshold on the sum of photonelectrons in an unoverlapping tile of 4x5 PMTs in RICH is required. A 4x5 tile could just cover the norminal size of a ring by an electron. Since the tiles are not overlapping, to enhance the efficiency, it's good to choose a relative low threshold. All the thresholds in the ERT trigger could vary run by run. For Run 8 d+Au data in this analysis, the equivalent thresholds before run 250515 are list as below: 2.8 GeV (PbSc) and 2.1 GeV (PbGl) for 4x4a, 3.5 GeV (PbSc) and 2.8 GeV (PbGl) for 4x4b, 2.1 GeV (PbSc) and 1.4 GeV (PbGl) for 4x4c, 600 MeV (PbSc) and 400 MeV (PbGl) for 2x2, and 3 photonelectrons for RICH. Fron run 250515, the 2x2 thresholds are raised to 800 MeV (PbSc) and 600 MeV (PbGl) according to the summary page at http://www.phenix.bnl.gov/WWW/trigger/pp/c-arm/Run3/run8.html.

A further Lever-2 (LVL2) trigger is used in the event assembling to enhance the interested physics data. An overview of LVL2 algorithms are summarized in Table 2.1.

The Min-Bias trigger loses the efficiency in the most peripheral collisions, because ZDCs could possiblly not able to get a coincidence on both sides.

2.2.2 Charged Particle Tracking

The central tracking system for charged particles consists of the Drift Chambers (DC), the Pad chambers (PC) and the Time Expansion Chamber (TEC). Two DCs are located on the east and west arm respectively,

Table 2.1: Overview of LVL2 trigger algorithm

Trigger	Method
Single Electron	Match RICH rings to EMCal clusters Make EMCal energy threshold cut
Electron Pair	Calculate invariant mass of electron pairs Make invariant mass cut
Single Muon	Calculate invariant mass of electron pairs Make invariant mass cut
Muon Pair	Find roads through MuID panels
High pT EMCal	Find EMCal clusters Make threshold cuts
High pT Charged	Match PC and DC hits Cut on the bend angle
Coherent Peripheral Events	Look for ZDC trigger with no BBC trigger Look for PC hits
Centrality Selection	Use BBC and ZDC to estimate centrality Make centrality cuts on selected triggers

each covers $\pi/2$ in azimuth. There are three layers of Pad Chambers, PC1, PC2, PC3 on the west arm, and PC1, PC3 and TEC on the east arm respectively. DCs provide high resolution measurements of the trajectory and momentum of the charged particles, PCs could provide 3D spacial point information for pattern recognition, and TEC tracks the charged particles between RICH and EMCal, identifies them by measuring dE/dX and improves the e/π separation. The multiplicity of charged particles in the central collisions at RHIC energy level is about $dN_c/d\eta = 700$ with a spectrum peaking at 200-300 MeV for soft particles. Due to the partial coverage in the azimuthal angle, a large number of charged particles enter the central tracking system without passing through DC. All the three detectors are essential to perform both an accurate measurement and a good pattern recognition in such a large multiplicity environment. STAR has a different configuration and would like to enjoy their barrel shaped Time Projection Chamber.

Drift Chamber

The Drift Chambers are cylinder shaped multiwire chambers, as shown in Figure 2.4. It locates at a radial distance from 2 m to 2.4 m, and it is 2 m along the beam axis. Thus each DC could cover 90° in azimuthal angle and ± 0.35 in pseudorapidity. DCs are outside of the central magnet field, and the residual magnetic field at DCs is about 0.6kG. The central magnet field is designed to be along the beam axis, therefore it only bent the charged particles in azimuth. Accordingly, DCs have better resolution in r-ϕ than z. The single wire resolution in r-ϕ is better than $150\mu m$, while the single wire resolution in z is designed to be better than $2mm$ only.

The volume of each DC detector on the east/west arm is confined by a cylinder Ti frame defined the azimuthal and z limits, also by Five-mil Al-mylar window defining the radial limits. Each frame is divided into 20 equal sectors, and each sector extends 4.5° in azimuth, as shown Figure 2.2.2.. In each sector are six types of wire modules positioned radially, namely X1, U1, V1, X2, U2 and V2. In each module, there are 4

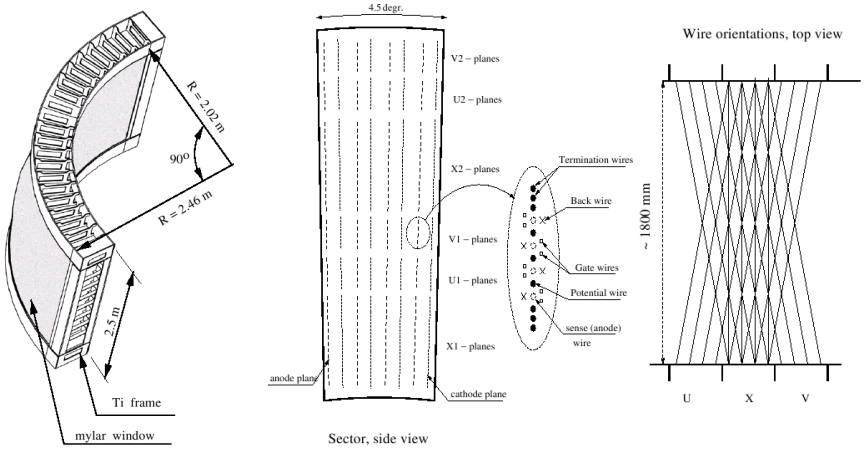

Figure 2.9: The frame of Drift Chamber (left), side view of the layout of wire arrangement in one sector and in one V1 anode plane (middle), top view of the wire orientation (right).

anode planes and 4 cathode planes. In the anode plane, there are other wires beside the anode wires. The anode wires are separated by the Potential wire, and surrounded by Gate wires and Back wires. Also, there are two Termination wires on both sides of the anode plane in each module. For X wire cells, there are 12 anode wires in each anode plane in a module, and for U, V wire cells, there are 4 anode wires in each plane, as shown in Figure 2.2.2..

The X wires are parallel to the beam pipe, and they are designed to have exellent resolution in r-ϕ plane. The U, V wires are placed with a small stereo angle (6°) respect to the X wires so that DCs are able to get the z position by those wires, see Figure 2.2.2.. The distance between the anode wires and the location where the electrons/ions are caused by the passing charged particle could be determined by the arrive time and the drift velocity in the working gas. In DC, the working gas is mixed by 50% Argone and 50% Ethane.

The track in Drift Chamber is reconstructed by a combinatorial Hough transform (CHT) technique. The Drift Chamber hits are mapped into a feature space which is defined by ϕ and α, as shown in Figure 2.10. ϕ is defined by the azimuthal angle of the crosspoint of the track trajectory and the middle radius of DC, while α is defined as the inclination angle of the track at that crosspoint. α is proportional to the inverse of pT such that it gives us a first estimation of the value of pT. X1, X2 hits are both required for the track reconstruction, and U, V hits are needed to determine z information.

Pad Chamber

After leaving the Drift Chamber, a charged particle enters a set of separate layers of Pad Chambers. They are in fact multiwire proportional chambers. The first layer PC1 is located betwee DC and RICH, about 2.45m away from the beam, which could determin the z coordinate at the outside of DC and make a good crosscheck with U, V wire readout in DC. The third layer PC3 is located just before EMCal, 4.9m away from the beam. The second layer PC2 is only installed in the wast central arm, as shown in Figure 2.4. PC2 and PC3 are needed to remove the particles which come from secondary interaction or hadron decay outside DC and finally enter EMCal. Also, low momentum charged particles which fly around DC and PC1 could be ruled out by PC2 and PC3 too. And the situation that three layer's hits in a straight line serves a good confirmation of a particle trajectory.

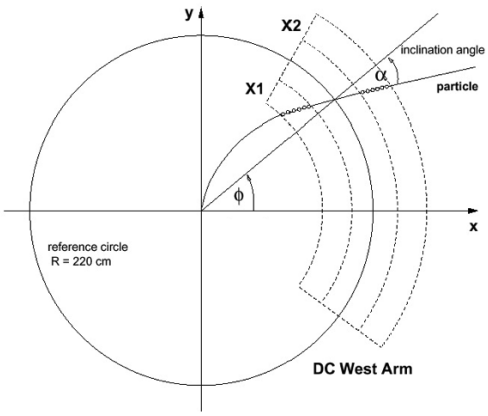

Figure 2.10: Illustration of the track reconstruction in Drift Chamber using CHT. The circles near the charged particle trajectory represent the Drift Chamber hits.

2.2.3 Photon Reconstruction

Electromagnetic Calorimeter

The Electromagnetic Calorimeters(EMCal or EMC) are primarily to measure the position, energy and time-of-flight information of photons and electrons/positrons in midrapdity region. Also, the quick response to energy deposition of EMCal is useful in triggering events with high pT photons and electrons. The underlying physics is that the photons and electrons interact with the medium by the electromagnetic shower, through cascading bremstrahlung(for electrons) and pair production(for photons, note: photonelectric effect and Compton scattering are only important when the energy of the incident particle is below a few MeV), while the hadrons deposit only a small fraction of the total energy by the hadronic shower, via strong interaction, which is more complicated. Two different detector technologies are adopted in PHENIX EMCal detector, one is lead scintillator calorimeters(PbSc), the other is lead glass Cherenkov detector(PbGl). PbSc is a sampling calorimeter, consisting layers of lead and scintillators; while PbGl is a homogeneous calorimeter, made of a whole lead-glass Cherenkov radiator. Such a configuration provides a valuable cross-check between two technologies with different characteristics. EMCal is the outmost of the PHENIX central arm, and is 5 meters away from the beam pipe. EMCal is composed of eight sectors. Six of them are PbSc detectors, and the other two are PbGl detectors. The PbSc has great signal linearity and timing response, and the PbGl has excellent energy resolution and granularity.

The PbSc detector consists of 15552 individual towers. Each tower is composed of 66 sampling cells which consists of alternating lead and scintillator layers. PMTs are attached in the backend, which are connected by optical fibers with those cells. A module of PbSc is composed of four individual towers, which are mechanically hold together. Thirty six modules are attached to a backbone and held together to form a supermodule(SM). A sector consists of eighteen supermodules. The energy resolution of PbSc is obtained by the beam test at BNL and CERN, and the fitted linear(A) and quadratic(B) resolutions are:

$$(\frac{\sigma_E}{E})_A = 1.2\% + \frac{6.2\%}{\sqrt{E(GeV)}} \tag{2.1}$$

$$(\frac{\sigma_E}{E})_B = 2.1\% \oplus \frac{8.1\%}{\sqrt{E(GeV)}} \tag{2.2}$$

The PbGl detector is previously serviced for CERN experiment WA98. Each PbGl sector comprises 192

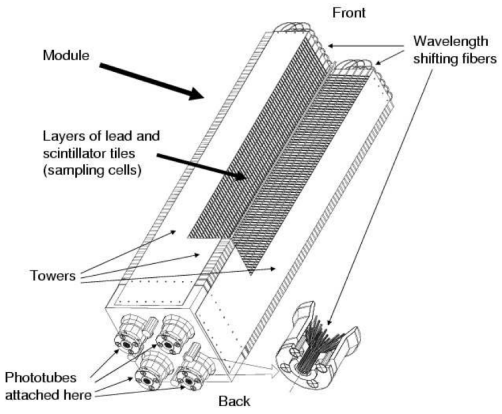

Figure 2.11: Interior view of a PbSc module

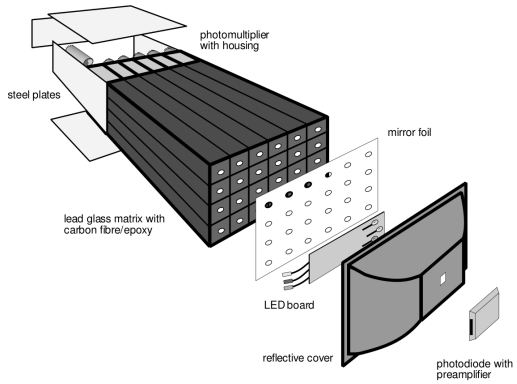

Figure 2.12: Exploded view of a PbGl supermodule

supermodules in an array of 16 SM in wide and 12 SM in height. Each supermodule consists of 24 modules in an array of 6 modules wide and 4 modules high. Each module is read out by a photomultiplier. The response of the PbGl has been studied in test beams of AGS at BNL and SPS at CERN. The energy resolution results are shown with the fit parameterization

$$\frac{\sigma(E)}{E} = \frac{[5.9 \pm 0.1]\%}{\sqrt{E/GeV}} \oplus [0.8 \pm 0.1]\% \tag{2.3}$$

The measured position resolution can be fitted with the parameterization

$$\sigma_x(E) = \frac{[8.4 \pm 0.3]mm}{\sqrt{E/GeV}} \oplus [0.2 \pm 0.1]mm \tag{2.4}$$

Muon Piston Calorimeter

Muon Piston Calorimeter (MPC) is a small lead-tungstate (PbWO4) based electromagnetic calorimeter with Avalanche Photodiode (APD) readout at the south and north side of PHENIX. It covers the rapidity in $3.1 < |\eta| < 3.9$, and the azimuth in 2π. MPC helps PHENIX to extend the acceptance to the forward/backward region and go further in the small x and spin physics. MPC is compact enough to be installed in the small hole just in front of the muon piston after which MPC is named, and strong enough to withold the magnetic field there. Each MPC are composed of 8 modules, as shown in 2.13, including 4 wedges (with 29 crystals each) and 4 bricks (with 19 crystals each). MPC consists of 192 crystals in total at each side.

2.2.4 Electron Identification

The Ring Imaging Cherenkov (RICH) detector, shown in Figure 2.14, is the principal electron ID device in PHENIX. The RICH detects the Cherenkov light ring produced by charged particles whose speed is faster than the speed of light in the medium, and measures the speed of that fast moving charged particle. If the momentum of the particle is provided, the mass of the particle could be derived and the type of particle could be identified. The RICH detector at PHENIX could identify the electrons above 18 MeV/c, and the Cherenkov threshold for charged pions is 4.65 GeV/c, which is much higher. Since the charged pions are the lightest charged hadrons, so any particles with momentum below 4.65 GeV/c detected by the RICH are electrons uniquely(Muons are rare). In this way, the RICH detector could be used to veto electrons from charged hadron tracks, which is useful in the hadronic jet analysis. The medium in the RICH detector is

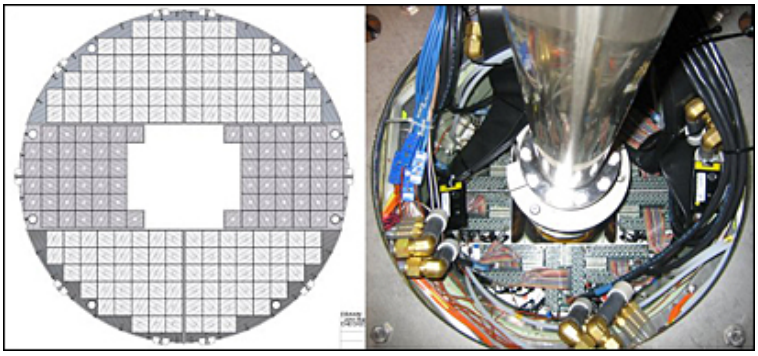

Figure 2.13: Muon Piston Clorimeter. Left: detector layout of the PbWO4 crystals; Right: MPC is installed around the beam pipe.

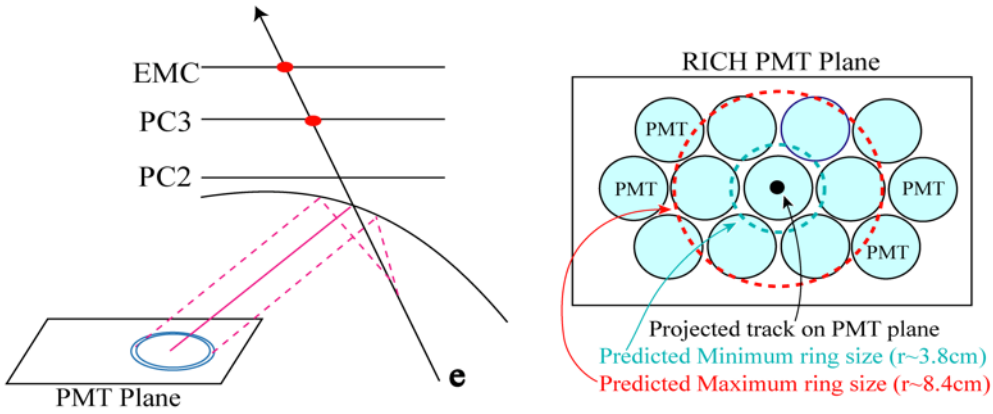

Figure 2.14: Electron signal depositions are shown in the RICH. Cherenkov radiation is reflected onto PMT array (left). Ring sizes are shown relative to PMT lattice (right).

CO_2 gas at 1 atm with refractive index 1.000410. The yield of Cherenkov light is determined by the length of the radiator medium, so the RICH detector is very large due to the gas vessel volume. The RICH detector produces about 12 photons in average for a $\beta \approx 1$ particle over a path length of 1.2 meters. To reduce the size of the radiation length, a set of very thin mirrors are mounted onto the PMT array, just outside the central arm η acceptance. There are 5120 PMTs in total mounted in the RICH detector.

Chapter 3

Analysis Procedure

3.1 PHENIX Data Set

Since 2000, PHENIX has collected data for each run period, see Table 3.1. In this analysis, Run8 dAu ERT triggered data are selected, and the number of events is about 10 million.

3.2 Particle Identification

3.2.1 Photon Identification

Clusters in the EMCal are identified as photons with these cuts:

- shower shape cut: $\chi^2 < 3$
- track-based charged hadron veto
- hot and dead tower exclusion
- fiducial cut: $|Z_{EMC}| < 155$ cm

The shower shape for electromagnetic shower and hadronic shower is much different. The EMCal detector response is predicted by the simulation with PISA(PHENIX Integrated Simulation Application, which is based on GEANT3 libraries), and a predict EM shower shape function for i-th tower(F_i) is perameterized as:

$$\begin{aligned} F_i &= \frac{E_i^{pred}}{E_{tot}} \\ &= P_1(E_{tot},\alpha)\exp\{-\frac{(r_i/r_0)^3}{P_2(E_{tot},\alpha)}\} + P_3(E_{tot},\alpha)\exp\{-\frac{(r_i/r_0}{P_4(E_{tot},\alpha)}\} \end{aligned} \tag{3.1}$$

Where, E_i^{pred} is the predicted energy of i-th tower, r_i is the distance between the center of i-th tower and corrected hit position, and r_0 is the surface size of a EMCal cell which is 5.5 cm. P_{1-4} are the parameterized

Table 3.1: A summary of PHENIX data sets through 2008.

RHIC Run (Year)	beam species	beam energy (GeV)	sampled events	$\int Ldt$
1 (2000)	Au+Au	130	10 M	1 μb^{-1}
2 (2001/2)	Au+Au	200	170 M	24 μb^{-1}
	p+p	200	3.7 B	0.15 pb^{-1}
3 (2002/3)	d+Au	200	5.5 B	2.74 nb^{-1}
	p+p	200	6.6 B	0.35 pb^{-1}
4 (2003/4)	Au+Au	200	1.5 B	241 μb^{-1}
	Au+Au	62.4	58 M	9 μb^{-1}
5 (2005)	Cu+Cu	200	8.6 B	3 nb^{-1}
	Cu+Cu	62.4	400 M	0.19 nb^{-1}
	Cu+Cu	22.4	9 M	2.7 μb^{-1}
	p+p	200	85 B	3.8 pb^{-1}
6 (2006)	p+p	200	233 B	10.7 pb^{-1}
	p+p	62.4	28 B	0.1 pb^{-1}
7 (2007)	Au+Au	200	5.1 B	813 μb^{-1}
8 (2008)	d+Au	200	160 B	80 nb^{-1}
	p+p	200	115 B	5.2 pb^{-1}

functions of total energy E_{tot} and impact angle α. P_{1-4} are obtained in the test beam run as

$$\begin{aligned} P_1 &= 0.59 - (1.45 + 0.13 \ln E_{tot}) \sin^2 \alpha \\ P_1 &= 0.27 - (0.80 + 0.32 \ln E_{tot}) \sin^2 \alpha \\ P_1 &= 0.25 - (0.45 + 0.036 \ln E_{tot}) \sin^2 \alpha \\ P_1 &= 0.42 \end{aligned} \tag{3.2}$$

Then the electromagnetic showers can be identified from the hadronic shower by the shower shape profile χ^2 test,

$$\chi^2 = \sum_i \frac{(E_i^{pred} - E_i^{meas})^2}{\sigma_i^2} \tag{3.3}$$

where E_I^{pred} is the measured energy in i-th tower after the calibration, E_i^{pred} is the predicted energy by Eq.3.1, and σ_i is the variance of the predicted energy function as

$$\sigma_i^2 = A \cdot E_i^{pred}(1 + B\sqrt{E_{tot}} \sin^4 \alpha)(1 - \frac{E_i^{pred}}{E_{tot}}) + q(E_{tot}) \tag{3.4}$$

where the constant A and B are obtained by the test beam data.

Although most of the hadronic shower is removed by the shower shape cut, there is still a considered number of hadron contamination. The photon candidate cluster are distinguished from the charged particles(electron converted by photon or remaining hadron) by associating the photon candidate clusters with charged particle hits in Pad Chamber (PC3), which is just 5 cm away in front of EMCal. The distance between hit positions of EMCal and PC3 is given by

$$r_{emc-pc3}^{veto} = \sqrt{dx_{emc-pc3}^2 + dy_{emc-pc3}^2 + dz_{emc-pc3}^2} \tag{3.5}$$

The threshold for charged particle veto is set to 6.5 cm based on the Moliere radius.

Any bad conditioned towers are recognized and removed by the hot/dead tower map. A tower with hit frequency higher/lower than 5σ of the averaged hit frequency per tower is tagged as a hot/dead tower. Any hot/dead tower with its 3x3 nearby towers are excluded from later analysis.

The fiducial cut on the edge could help to rule out the photons which are unable to be reconstructed correctly due to part of their energy is not deposited into EMCal.

The efficiency of photon identification cut is NOT studied for now, and should be done by simulation.

3.2.2 π^0 and η Identification

π^0 and η are neutral mesons which can decay into photons. They are reconstructed by the invariant mass of photon pairs by

$$\begin{aligned} m_{inv} &= \sqrt{(E_1+E_2)^2-(\mathbf{p}_1+\mathbf{p}_2)^2} \\ &= \sqrt{2E_1E_2(1-\frac{x_1x_2+y_1y_2+z_1z_2}{l_1l_2})} \\ &= \sqrt{2E_1E_2(1-\cos\psi)} \end{aligned} \tag{3.6}$$

where ψ is the opening angle between the two photons' tracks, E_i is the energy of photon i, $\mathbf{p}_i$ is the momentum of photon i, x_i, y_i, z_i are the coordinates of photon i, l_i is the path length from the collision vertex which is determined by BBCs to the hit position of photon i. The reconstructed invariant mass should be within the mass window for pi^0 or η mesons. The invariant mass spectrum of the photon pairs could be fitted by a gaussian peak of the "real" π^0 and a 3rd order polynomial of fake pi^0 from the combinatorial background. The mass window for π^0 is 120-160MeV, and that for η is 530-580MeV. To reduce the combinatorial background, the two photons' energy should be greater than 1GeV, which help to remove the soft photons, the major source of the combinatorics. For high pT photons which decay from the same π^0 are likely not to separate far away and to remain in the same sector of EMCal, while the random combinatorial matching of photon pairs has no such trends. Accordingly, the sub-leading photon is required to be in the same sector as the leading photon. Also, at high pT region, most fake π^0s are due to the random combination of a high pT(must be high energy) photon which comes from a real π^0 and a low energy soft photon. They could possibly be distinguished by the concept of asymmetry:

$$asymmetry = \left|\frac{E_1-E_2}{E_1+E_2}\right| \tag{3.7}$$

The asymmetry cut on the photon pairs could alleviate the random combinatorial π^0 match problem. The threshold is determined by both energy of the photons and the centrality of the event. The background from combinatorial match for π^0 is pretty small from simulation. The contribution from false match for η should be removed by sideband analysis. Since the η meson is not yet included in current consideration, such a subtraction is not performed and would not be discussed here.

3.2.3 Charged Hadrons Identification

The reconstructed tracks in the drift chamber are identified as charged hadron tracks based on the following criteria:

- Track quality

- PC3 and EMCal matching
- RICH ring veto
- Drift chamber z-edge cut
- EMCal energy cut

In a high multiplicity environment, fake tracks could be reconstructed by unrelated hits in the tracking system, or, the real tracks constructed could lack hitting point in some detectors. Accordingly, the quality control in the charged track reconstruction is a important part of the analysis. In PHENIX tracking system, six bits, shown below, are used to describe the quality of the reconstructed tracks.

◇ bit 0 (1): X1 used

◇ bit 1 (2): X2 used

◇ bit 2 (4): UV found

◇ bit 3 (8): UV unique

◇ bit 4 (16): PC1 found

◇ bit 5 (32): PC1 unique

The tracks with quality bit of 63 or 31 are selected in this analysis(in makeMNSingles, and quality > 7 in process_event, which require sufficient X1, X2 and UV hits). Quality 63 means hits in X1, X2 and UV wires in DC and also a unique hit in PC1, while quality 31 doesn't require PC1 hit to be unique.

The DC/PC1 hit matching with quality selection is not a guarantee to erase the "ghost" particles which are just random matching between them. Also the background from off-vertex tracks, such as the tracks from conversion, deflection and decay, should be excluded from our analysis since the current charged track analysis assumes that all tracks are from the collision vertex. Due to these consideration, the outer PC layers are included into the charged particle selection cuts. Since PC2 is only installed on west arm, only PC3 is incorporated into the analysis at this moment. Along with the magnetic field consideration, the tracks reconstructed from DC and PC1 hit are projected to PC3, and the projection point should match a nearby PC3 hit. The matching window is determined by a Gaussian fit of the distance between the projection point and the PC3 hit position, and the PC3 matching cut is appropriately selected as 3σ of the normalized Gaussian peak, or $\sqrt{\sigma^2_{\Delta\phi} + \sigma^2_{\Delta z}} < 3$. Actually it is a double Gaussian fit because the real match and random combinatorics have their own Gaussian peaks. The EMCal matching is pretty similar to PC3 matching mentioned above.

Electrons are rejected by vetoing from the RICH ring. Any charged particle except electrons with pT less than 4.65 GeV/c is unable to radiate Cherenkov light in the RICH detector, and a zero coincidence with RICH radiation rings, a.k.a. $n0 \leq 0$, serves as a cut for charged tracks with pT below this value. If the charged particle's pT is greater than this threshold, it could still radiate Cherenkov rings based on its mass. The pions radiate first at or just above this threshold, then other heavier charged particles radiate with even higher pT. If the charged particle is above its threshold for radiating in RICH, a e/p ratio cut in EMCal is applied. In this cut, the ratio between the energy deposited in EMCal by this particle and its own momentum is calculated and should below a specific value (Currently no in the CombinedSimple code).

It's possible that a charged particle hits the edge region of DC and crosses out of its side boundary. To prevent this case which would bring unexpected errors into the charged particle efficiency estimation, a fiducial cut of z-edge cut of DC is applied as shown below

- ◇ West arm: $-0.54 < \phi_{DC} < 0.92$
- ◇ East arm: $2.25 < \phi_{DC} < 3.65$
- ◇ $Z_{ed} < 75cm$
- ◇ $the0 < 0$

wher ϕ_{DC} and Z_{ed} are the ϕ and z coordinates of the hit position on DC respectively, and $the0$ is the polar angle θ of the reconstructed track from the collision vertex which is determined by the BBC detectors.

3.3 Two Particle Correlation

For heavy ion collisions, even for p+p or d+A collisions, the large amount of soft particles makes the direct jet reconstruction difficult. For the existing jet reconstruction methods, they are forced to use particles with high pT value(as large as several GeV) to avoid the soft particles background. If we include these particles, the jet would be too broad and include the contamination from "underlying events". The situation is even complicated by the limited acceptance of PHENIX detector, because the central arm can detect the particles with $|\eta| < 0.35$ which leads that some of the jet constituents are leaked outside of the detector acceptance.

The two-particle azimuthal correlation method is an alternative tools to investigate the jet property. It is based on the fact that in Leading-Order QCD, the outgoing partons in hard scattering events are back-to-back, both in azimuthal angle and polar angle (a.k.a. rapidity). Any deviation from this should be a result from the Next-to-Leading-Order effect, soft gluon radiation, multiple scattering or the response from the medium. With carefully chosen variables, the contribution from different effects could be distinguished by the two-particle azimuthal correlation method. The result from d-A collisions serves as a base-line for comparing with A-A, and could make a clear view of the separate contributions of the deviations coming from hot dense medium and cold nuclear medium. In two-particle azimuthal correlation method, a high pT($\geqslant 5GeV/c$) trigger, either a photon or a π^0 is chosen as a trigger. Within this particular pT range for the trigger, if the trigger is a direct photon, it is likely either coming directly from the hard scattering process for the prompt photon, or near or part of the jet, which is the fragmentation products of a hard scattering parton, for a decay photon or a π^0. Actually, most of decay photons come from the decay mode of π^0s as $\pi^0 \rightarrow \gamma + \gamma$. In the other hand, the charged hadrons with relative high pT($\geqslant 1GeV/c$) value are chosen as the associated partners. The pT threshold for the associated particles helps to remove some of the soft particle background which comes from the underlying events. Due to the nature of the hard scattering events, the trigger and the associated particles tends to swarm together or to fly apart almost back-to-back. This could be clearly visualized by looking at the distribution of the azimuthal angle differences between the trigger and the associated particles, as shown in Figure 3.1. The two peaks in $\Delta\phi$ distribution of the two-particle correlation are corresponding to the near- and away-side jets to which the associated partner hadron belongs. The so called near- and away-side are relative to the trigger's direction.

Actually, the rapidity/pseudorapidity η correlation is realized and identified, as shown in Figure 3.2. The broadening in $\Delta\eta$ in the near-side correlation in Au+Au collision is refered as "ridge". The suppresion at $\Delta\phi = \pi$ is refered as "head", while the enhancement at $\Delta\phi = \pi \pm 1.1$ is refered as "shoulder". The head

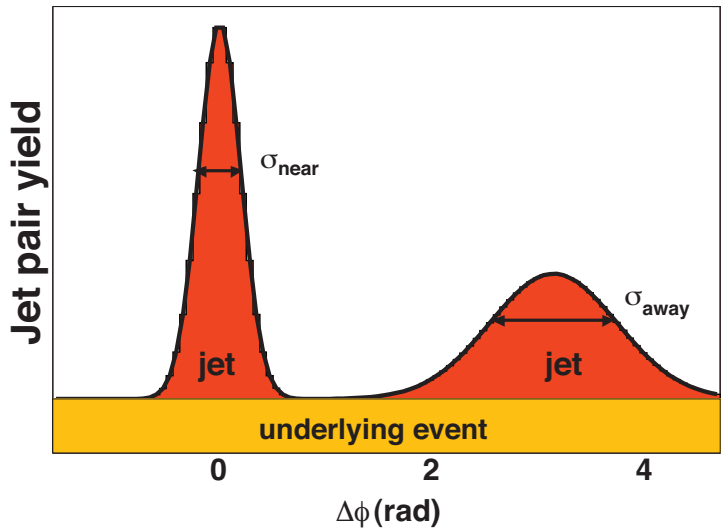

Figure 3.1: Cartoon plot of two-particle correlation distribution in $\Delta\phi$ for d+Au collisions. The two peaks are due to the near- and away-side jets. The flat pedestal comes from the underlying events background.

results from the jet suppresion in heavy-ion collision due to the existence of hot dense medium, and the should is generally suggested by originating from the medium response. The studies in these different regions could render us a good understanding of the interaction between the parton and the medium, therefore give us a glance at the properties of the medium and QCD processes. However, the limited η acceptance in PHENIX central arms, see Figure 2.3, prevents further studies. Recent installation of Muon Piston Calorimeter (MPC) detector would help to boost such studies and expand our knowledge in jet correlations and medium response in heavy ion collision. Currently, no η is applied in this analysis.

3.3.1 Notations for Mathematical Framework

To make a clear introduction, this subsection is going to show the notations used in the derivation of the mathematical framework for the two-source model of jet correlation physics. All of them are following PHENIX Analysis Notes 646 [15].To make things easy, we would like to look at the symbols and units at first.

$$[N] = counts \tag{3.8}$$

$$[\mathbb{N}] = raw\ counts \tag{3.9}$$

$$[n] = counts/event \tag{3.10}$$

$$[\mathbb{n}] = raw\ counts/event \tag{3.11}$$

$$\left[\frac{dn}{d\Delta\phi}\right] = counts/event/rad \tag{3.12}$$

$$\left[\frac{d\mathbb{n}}{d\Delta\phi}\right] = raw\ counts/event/rad \tag{3.13}$$

The capital letter denotes total counts, while the letter in small case denotes per-event quantity. The blackboard bold letter means measured quantity, while the regular letter means the true quantity. Then the

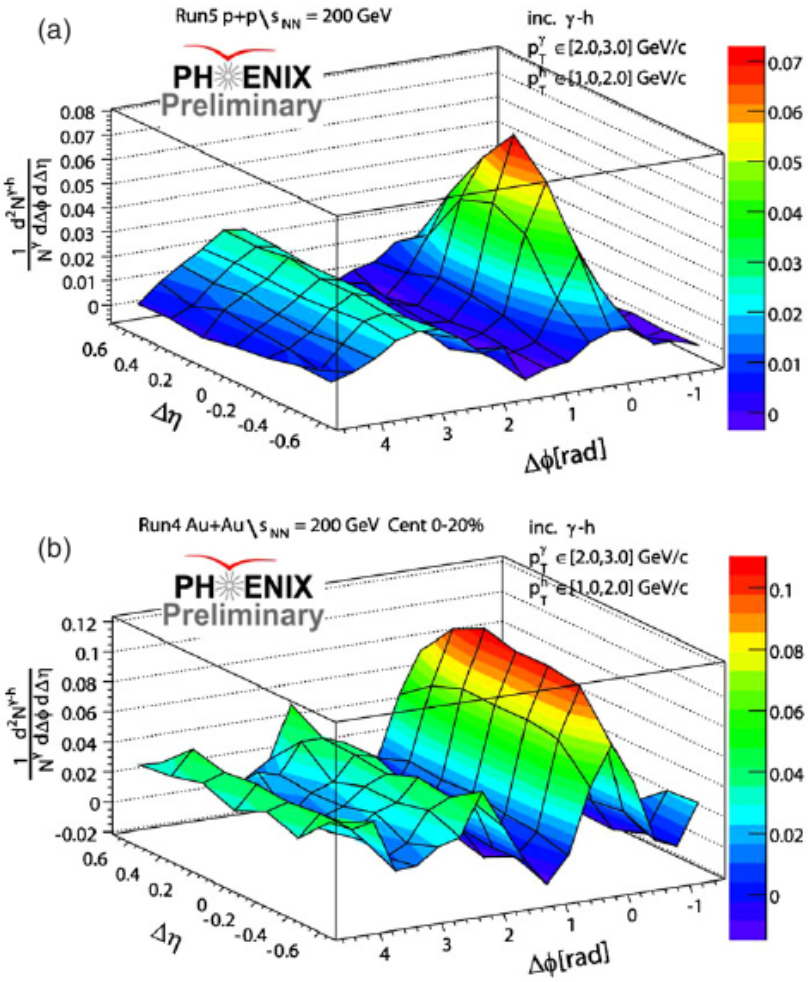

Figure 3.2: Per-trigger yields for inclusive photon, $2 < p_T^{\gamma} < 3GeV/c$, paired with charged hadron partners, $1 < p_T^h < 2GeV/c$, in p+p and Au+Au collisions respectively in (a) and (b) [16]

efficiencies are defined as

$$\mathfrak{n}^A = \epsilon^A n^A \tag{3.14}$$

$$\mathfrak{n}^B = \epsilon^B n^B \tag{3.15}$$

$$\mathfrak{n}^{AB}_{real} = \epsilon^{AB}_{real} n^{AB}_{real} \tag{3.16}$$

$$\mathfrak{n}^{AB}_{mixed} = \epsilon^{AB}_{mixed} n^{AB}_{mixed} \tag{3.17}$$

The superscript A means the trigger(photon or pion), B means the associated partner(charged hadron), and AB means a two-particle pair formed by the trigger and the partner. The subscription $real$ means that it is a quantity from real events, and $mixed$ means that it comes from mixed events. The single particle efficiencies could be obtained by comparing the raw counts and the published PHENIX data instead of full Monte Carlo simulations.

3.3.2 Acceptance Correction and Event Mixing

The $\Delta\phi$ distribution of the two-particle correlation quantities should be corrected because of the uneven acceptance efficiency on different $\Delta\phi$ value, which results from the limited PHENIX azimuthal acceptance,

shown in Figure 2.3, as well as the working condition of the detector subsystems of PHENIX and the application of various cuts in event and particle selection. To address this issue, a common procedure is to mix up different events which belong in the same group with similar characteristics, such as the centrality. Since the two particles in the pair are from different events, they are unlikely to be correlated. (Even though, there might be some unknown residual correlation existing, such as correlation with the reaction plane.) The shape of the $\Delta\phi$ distribution from the mixed events only arises from the acceptance efficiency. Following this idea, if we divide the real event distribution of N^{pair}_{real} by the mixed event distribution of N^{pair}_{mixed}, we might be able to cancel out and correct the uneven $\Delta\phi$ acceptance efficiency, which is largely due to the limited PHENIX azimuthal acceptance. Therefore, the correlation function $C\left(\Delta\phi\right) \equiv N^{pair}_{real}(\Delta\phi)/N^{pair}_{mixed}(\Delta\phi)$ is a good choice in the two-particle jet correlation analysis. The correlation function $C(\Delta\phi)$ could also be normalized by the integrated yields and redefined as,

$$C(\Delta\phi) \equiv \frac{\frac{d\mathbb{n}^{AB}_{real}}{d\Delta\phi}}{\frac{d\mathbb{n}^{AB}_{mixed}}{d\Delta\phi}} \frac{\int \frac{d\mathbb{n}^{AB}_{mixed}}{d\Delta\phi} d\Delta\phi}{\int \frac{d\mathbb{n}^{AB}_{real}}{d\Delta\phi} d\Delta\phi} \tag{3.18}$$

The acceptance correcton is defined as

$$\frac{dn^{AB}_{real}}{d\Delta\phi} = \frac{\frac{d\mathbb{n}^{AB}_{real}}{d\Delta\phi}}{Acc(\Delta\phi)} \tag{3.19}$$

which is used to get the real number of the trigger-partner pairs. And the reason why we need the mixed events lies here. By using the sum rule from [17],

$$\int C(\Delta\phi) d\Delta\phi = \frac{\epsilon^{AB}_{mixed}}{\epsilon^{AB}_{real}} \int d\Delta\phi \tag{3.20}$$

the acceptance correction is derived to be

$$Acc(\Delta\phi) = \frac{d\mathbb{n}^{AB}_{mixed}}{d\Delta\phi} \frac{\epsilon^{AB}_{mixed}}{\mathbb{n}^{AB}_{mixed}} \int d\Delta\phi \tag{3.21}$$

ϵ^{AB} is essential for the evaluation of acceptance correction. To determine its value, we look at the multiplicity for mixed events

$$\mathbb{n}^{AB}_{mixed} = \kappa \mathbb{n}^{A} \mathbb{n}^{B} \tag{3.22}$$

$$n^{AB}_{mixed} = n^{A} n^{B} \tag{3.23}$$

κ is the pair efficiency due to the cuts in our analysis, then, we get

$$\epsilon^{AB}_{mixed} = \kappa \epsilon^{A} \epsilon^{B} \tag{3.24}$$

In this way, the acceptance correction could be achieved by the event mixing and the evaluation of those efficiencies.

3.3.3 Two-Source Model and Combinatorial Background

As in the direct jet reconstruction, the soft background products still play a role in the two-particle correlation analysis. Apart from the jet correlation, the random combination of uncorrelated particles, at least uncorrelated through the hard scattering (or say, the partner hadrons come from the underlying events), build up the pedestal background. The correlation function could be decomposed into two parts, one from the

pair yields of two-particle jet correlation, the other from the combinatorial background from the underlying events.

$$\frac{dN^{AB}_{real}(\Delta\phi)}{d\Delta\phi} = \frac{dN^{AB}_{comb}(\Delta\phi)}{d\Delta\phi} + \frac{dN^{AB}_{jet}(\Delta\phi)}{d\Delta\phi} \tag{3.25}$$

using per event,

$$\frac{dn^{AB}_{real}(\Delta\phi)}{d\Delta\phi} = \frac{dn^{AB}_{comb}(\Delta\phi)}{d\Delta\phi} + \frac{dn^{AB}_{jet}(\Delta\phi)}{d\Delta\phi} \tag{3.26}$$

The correlation function $C(\Delta\phi)$ could have other variants, such as the one normalized by the number of events or even by the number of triggers. Per event quantities and per-trigger quantities are two common way to evaluate the azimuthal correlations. In this analysis, the different types of triggers have different efficiencies. By using the per-trigger quantities, we are about to remove such difference across the different trigger types because dividing the pair number related quantities by the number of triggers can cancel the trigger efficiency. This advantage gets more prominent, especially when the direct photon result is obtained by subtracting the decay photon result (which is derived from π^0 meson result) from the inclusive one. Therefore we define the per-trigger yield (PTY),

$$\frac{1}{n^A}\frac{dn^{AB}}{d\Delta\phi} = \frac{1}{n^A}\left[\frac{dn^{AB}_{jet}}{d\Delta\phi} + \frac{dn^{AB}_{comb}}{d\Delta\phi}\right] \tag{3.27}$$

using the measurable quantities

$$\frac{1}{n^A}\frac{dn^{AB}_{jet}}{d\Delta\phi} = \frac{\epsilon^A}{\mathbb{n}^A}\left[\frac{\frac{d\mathbb{n}^{AB}_{real}}{d\Delta\phi}}{Acc(\Delta\phi)} - \frac{dn^{AB}_{comb}}{d\Delta\phi}\right] \tag{3.28}$$

The only remaining part is the combinatorial background term. It could be evaluated by various methods, such as the zero yields at minimum (ZYAM) method and absolute subtraction (ABS) methods.

The idea of ZYAM is that we assume the pair yield of the jet correlation approaches to zero at some minimum point $\Delta\phi_{min}$, *i.e.*

$$\left.\frac{dn^{AB}_{comb}}{d\Delta\phi}\right|_{\Delta\phi_{min}} = 0 \tag{3.29}$$

The minimum value for PTY corresponds to the combinatorial background from dAu collision which has no elliptical flow, since it is only a constant value without any v_2 term. The jet correlation could be fitted by two Gaussian peak after subtraction of the combinatorial backgrounds.

The effectiveness of ZYAM could be impaired by the situation lacking of statistics, such as the region $\Delta\phi$ near $\pi/2$ in high pT bins either for the trigger or the associated partners.

In the ABS methods, we assume that the multiplicity of combinatoric pairs in the real event could be represented by the one in mixed events after a centrality-multiplicity correlation correction. The mixed event method counts the pair multiplicity in mixed events

$$\mathbb{n}^{AB}_{comb} = \mathbb{n}^{AB}_{mixed} \cdot \xi \tag{3.30}$$

divided by ϵ^{AB}_{mixed}, we get similar form,

$$n^{AB}_{comb} = n^{AB}_{mixed} \cdot \xi \tag{3.31}$$

or the differential form,

$$\frac{dn^{AB}_{comb}(\Delta\phi)}{d\Delta\phi} = \frac{dn^{AB}_{mixed}(\Delta\phi)}{d\Delta\phi} \cdot \xi \tag{3.32}$$

The mean-seeds mean-partner method (MSMP) could be derived by using Equation 3.22. It measures the single particle multiplicity and the pair cut loss in mixed events.

$$\mathbb{n}^{AB}_{comb} = \mathbb{n}^{A}\mathbb{n}^{B}\kappa \cdot \xi \tag{3.33}$$

In d+Au collision, the combinatorial background is a constant over all $\Delta\phi$, so

$$\frac{d\mathbb{n}^{AB}_{comb}(\Delta\phi)}{d\Delta\phi} = \frac{\mathbb{n}^{A}\mathbb{n}^{B}\kappa \cdot \xi}{\int d\Delta\phi} \tag{3.34}$$

consequently,

$$\frac{dn^{AB}_{comb}(\Delta\phi)}{d\Delta\phi} = \frac{\mathbb{n}^{A}}{\epsilon^{A}}\frac{\mathbb{n}^{B}}{\epsilon^{B}}\frac{1}{\int d\Delta\phi} \cdot \xi \tag{3.35}$$

The introducing of ξ roots in the fact that the central events contribute more pairs than the peripheral events, or say the multiplicity is uneven with the centrality. In the process of event mixing, the events within the same centrality bin(see Line 200 of combOnetrigbgTrack.C) are randomly selected for mixing. The event on the up edge of the centrality bin is under-weighted for the multiplicity by event mixing procedure. "The correction modifies the background level by $\approx 0.2\%$ in the most central and $\approx 25\%$ in the most peripheral Au+Au collisions" according to [18]. To determine the value of ξ, we start from the integrated two-particle pair yield in mixed events

$$\int \frac{dN^{AB}_{mixed}(\Delta\phi)}{d\Delta\phi}\, d\Delta\phi = N^{AB}_{mixed} = N^{evt}_{mixed}\, n^{A} n^{B} \tag{3.36}$$

then based on the two-source model Equation 3.25, we could decompose the two-particle pair yield into the jet correlation part and the combinatorial background

$$\frac{dN^{AB}_{real}(\Delta\phi)}{d\Delta\phi} = \frac{dN^{AB}_{jet}(\Delta\phi)}{d\Delta\phi} + N^{evt}_{real}\frac{dn^{AB}_{comb}(\Delta\phi)}{d\Delta\phi} \tag{3.37}$$

using Equation 3.32

$$\frac{dN^{AB}_{real}(\Delta\phi)}{d\Delta\phi} = \frac{dN^{AB}_{jet}(\Delta\phi)}{d\Delta\phi} + N^{evt}_{real} \cdot \xi \cdot \frac{dn^{AB}_{mixed}(\Delta\phi)}{d\Delta\phi} \tag{3.38}$$

integrated by $\Delta\phi$

$$N^{AB}_{real} = N^{AB}_{jet} + N^{evt}_{real} \cdot \xi \cdot n^{AB}_{mixed} \tag{3.39}$$

by using Equation 3.23

$$N^{AB}_{real} = N^{AB}_{jet} + N^{evt}_{real} \cdot \xi \cdot n^{A} n^{B} \tag{3.40}$$

Also, as we discussed above, the combinatorial background comes from the residual correlation from the finite centrality bin, we could write

$$N^{AB}_{real} = N^{AB}_{jet} + N^{evt}_{real}\langle n^{A}(c)\, n^{B}(c)\rangle \tag{3.41}$$

Here the second term stands for the residual correlation in the mixed events, arising from the finite centrality bin correlation. Therefore the angle brace means the average value over the centrality bin, and n^{A}, n^{B} are the functions of the centrality c. Comparing the two equations above, we derive [9]

$$\xi = \frac{\langle n^{A}(c)\, n^{B}(c)\rangle}{n^{A}\, n^{B}} \tag{3.42}$$

3.4 Statistical Subtraction

Event-by-event direct photon analysis is still hard for Au-Au collision due to the high multiplicity environment and the limited acceptance of PHENIX detector. A naive idea is to get the direct photons by subtracting the decay photons from the inclusive photons. Even this idea is complicated by the fact that we can't tell if a single photon comes from decay or not. Statistical subtraction is an alternative and feasible method to study direct photons and related quantities such as gamma-hadron correlation per-trigger yield. The fraction of direct photon and decay photon in the inclusive photon sample is expressed by the quantitiy R_γ,

$$R_\gamma \equiv \frac{N^\gamma_{inclusive}}{N^\gamma_{decay}} \tag{3.43}$$

R_γ could be obtained from other measurements in PHENIX. The per-trigger yields (PTYs) of the inclusive, decay, derect photon have the relation as

$$N^\gamma_{inclusive} \cdot Y_{inclusive} = N^\gamma_{direct} \cdot Y_{direct} + N^\gamma_{decay} \cdot Y_{decay} \tag{3.44}$$

Here, we use Y denotes the per-trigger yield.By reformatting and using $N^\gamma_{inclusive} = N^\gamma_{direct} + N^\gamma_{decay}$, we found

$$Y_{direct} = \frac{1}{R_\gamma - 1}\left(R_\gamma Y_{inclusive} - Y_{decay}\right) \tag{3.45}$$

The contribution from decay photons to γ-hadron correlation is estimated from the π^0s by a statistical method. Currently η is not considered, although the same procedure is applied for it. The basic idea is this weighting function

$$\frac{d\mathbb{N}^\gamma_{decay}(p^\gamma_T)}{dp^\gamma_T} = \int \epsilon_\gamma(p^\gamma_T, p^\pi_T) \cdot P(p^\gamma_T, p^\pi_T) \cdot \frac{1}{\epsilon_\pi(p^\pi_T)} \cdot \frac{d\mathbb{N}^\pi(p^\pi_T)}{dp^\pi_T} dp^\pi_T \tag{3.46}$$

ϵ_γ and ϵ_π are the single particle efficincies for γ and π^0, which could be obtained by compairing the single particle counts with the published data in PHENIX. P is the decay probability density for a π^0 with p^π_T to decay into a photon with p^γ_T. Equation 3.46 is for the decay photon yields, similarly, for the decay γ-h pair yields the weighting function looks like

$$\frac{d\mathbb{N}^{\gamma-h}_{decay}(p^\gamma_T)}{dp^\gamma_T} = \int \epsilon_\gamma(p^\gamma_T, p^\pi_T) \cdot P(p^\gamma_T, p^\pi_T) \cdot \frac{1}{\epsilon_\pi(p^\pi_T)} \cdot \frac{d\mathbb{N}^{\pi-h}(p^\pi_T)}{dp^\pi_T} dp^\pi_T \tag{3.47}$$

Ideally, the integration should range from 0 to ∞, though in the collisions with the energy $\sqrt{s}$ in the center of mass frame, the π^0-h pair goes to 0 as p^π_T approaches $\sqrt{s}/2$. Pratically, due to the limitation of the detector's capability, we have to perform some truncation at some p_T threshold.

In the two-particle correlation analysis, the pT values of the particles are pretty high compared with their mass, $m_\gamma = 0$ and $m_\pi = 0.135GeV$. Considering that the position of EMCal is in the central region of PHENIX, we could safely state that the energy of the photon/pion is close to its pT value. With the approximation assumption that the probability of π^0 with p^π_T decaying to a γ is nearly flat in possible γ energy/pT range $0 \lesssim E_\gamma \lesssim p^\pi_T$, then the probability density should be roughly $\frac{dN^\gamma}{dp^\gamma_T} \approx \frac{2}{p^\pi_T}$. In this two-particle correlation analysis, four finite trigger pT bins are chosen to study. Therefore, for such a decay photon pT bin, $a < p^\gamma_T < b$, the probability could be derived as

$$P_y(\, p^\pi_T \,|\, a < p^\gamma_T < b\,) \equiv \int_a^b P(p^\gamma_T, p^\pi_T)\, dp^\gamma_T = \begin{cases} 0\,, & p^\pi_T < a \\ \int_a^{p^\pi_T} \frac{2}{p^\pi_T}\, dp^\gamma_T = 2(1 - \frac{a}{p^\gamma_T})\,, & a < p^\pi_T < b \\ \int_a^b \frac{2}{p^\pi_T}\, dp^\gamma_T = 2(\frac{b-a}{p^\pi_T})\,, & p^\pi_T > b \end{cases} \tag{3.48}$$

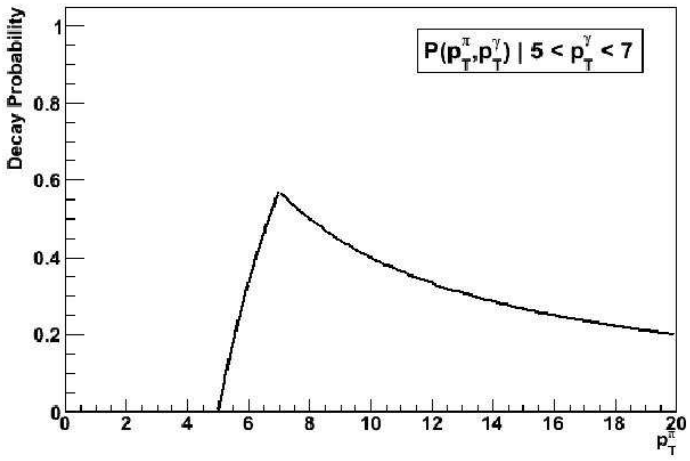

Figure 3.3: Probability for a π^0 decay into a photno with $5 < p_T^\gamma < 7$

The function is show in Figure 3.3, for a=5 Gev/c and b=7 Gev/c. Although this analytic function is based on the assumption that the detector should be perfect (no efficiency problem, and π^0 is flat on pT and z), it already shows some key characteristics of the decay kinematics. It arises sharply in the region of (a, b), then descends slowly as p_T^π gets higher.

For practice, however, the detector acceptance, resolution and π^0 identification cuts could make things more complicated. In this context, altogether, they are refered as π^0 reconstruction efficiency collectively. The π^0 efficiency pT distribution is much different with γ. From previous MC study [19], the π^0 efficiency rises rapidly in low pT region about $1-5 GeV/c$ and remains almost constant until a high pT range($< 12 GeV/c$), see Figure 3.4. Later studies show that the π^0 efficiency suffers a dramatical loss at even higher pT($> 12 GeV/c$) due to merging effect, because the opening angle between the two decay photons is so small compared to the size of the EMCal towers in such a high pT range. The π^0 efficiency changes as pT, while the γ efficiency is almost flat except the merging effect in high pT region for decay photons(This would enhance the direct photon fraction in the inclusive sample at this high pT region). Besides this momentum distrubtion difference, π^0 efficiency differs with γ position as well as its own momentum. At the edge of detector, π^0 efficiency drops due to one of the daughter photon might be lost outside the detector acceptance. A more detailed version of Equation 3.46 should be used

$$\mathbb{N}^\gamma_{a-b} = \int_a^b dp_T^\gamma \int dz^\gamma \int_0^\infty dp_T^\pi \int dz^\pi \, \frac{1}{\epsilon_\pi(p_T^\pi, z^\pi)} \frac{d^2\mathbb{N}^\pi(p_T^\pi, z^\pi)}{dp_T^\pi \, dz^\pi} P(p_T^\pi, z^\pi, p_T^\gamma, z^\gamma) \epsilon_\gamma(p_T^\pi, p_T^\gamma, z^\gamma) \tag{3.49}$$

Using the assumption that π^0 distribution on z is flat, which could be justified by the limited η acceptance of the central arm, we could simplify it

$$\mathbb{N}^\gamma_{a-b} = \int_a^b dp_T^\gamma \int dz^\gamma \int_0^\infty dp_T^\pi \int dz^\pi \, \frac{1}{\epsilon_\pi(p_T^\pi, z^\pi)} \frac{d\mathbb{N}^\pi(p_T^\pi)}{dp_T^\pi} P(p_T^\pi, z^\pi, p_T^\gamma, z^\gamma) \epsilon_\gamma(p_T^\pi, p_T^\gamma, z^\gamma) \tag{3.50}$$

The single decay photon efficiency ϵ_γ is evaluated by GEANT simulation. If we combine it with the decay probability density,

$$W(p_T^\pi, z^\pi, p_T^\gamma, z^\gamma) \equiv P(p_T^\pi, z^\pi, p_T^\gamma, z^\gamma) \epsilon_\gamma(p_T^\pi, p_T^\gamma, z^\gamma) \tag{3.51}$$

$$W_{a-b}(p_T^\pi, z^\pi, z^\gamma) \equiv \int_a^b dp_T^\gamma \, W(p_T^\pi, z^\pi, p_T^\gamma, z^\gamma) \tag{3.52}$$

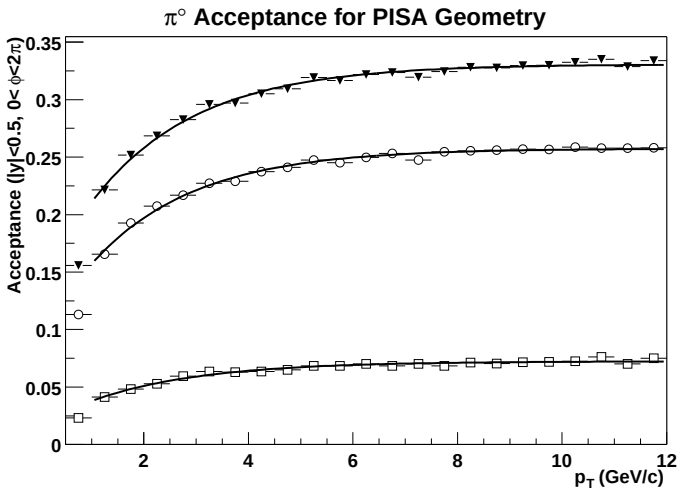

Figure 3.4: EMCal(solid triangles), PbSc(empty circles) and PbGl(empty squares) $\pi^0 \to \gamma\gamma$ acceptances(per unit rapidity and full ϕ) as a function of p_T^π based on Run 2 PISA geometry. The solid lines are the fitted results.

then

$$\mathbb{N}^\gamma_{a-b} = \int_a^b dp_T^\gamma \int dz^\gamma \int_0^\infty dp_T^\pi \int dz^\pi \frac{1}{\epsilon_\pi(p_T^\pi, z^\pi)} \frac{d\mathbb{N}^\pi(p_T^\pi)}{dp_T^\pi} W(p_T^\pi, z^\pi, p_T^\gamma, z^\gamma) \tag{3.53}$$

The decay γ-h per-trigger yield could be expressed as Equation 5 in [20]

$$PTY_{decay}\Big|_{a<p_T^\gamma<b} = \frac{\sum_{i=1}^{N^{\pi-h}} W_{a-b}(p_T^{\pi_i})/\epsilon_\pi(p_T^{\pi_i})}{\sum_{i=1}^{N^\pi} W_{a-b}(p_T^{\pi_i})/\epsilon_\pi(p_T^{\pi_i})} \tag{3.54}$$

The equation 3.54 from the reference [20] is kindof different with the definition above for W and ϵ_π. I will try to derive and interpret it later in Section 3.5.

For two-particle correlation analysis, the per-trigger pair yields are in deed calculated. Thus, the efficiency ratio between the two-particle pair and the trigger should keep the same level for both the inclusive and the decay photon for the purpose of a proper subtraction. It imposes the same requirement on the π^0 efficiency ratio. However, it is not always true, especially near the edge of the detectors. A large fraction of the associated hadrons on the near-side could be lost if the trigger is close to the edge. As mentioned above, π^0 is less reconstructed near the edge, so it suffers less in the per-trigger yield. Then it causes a over-subtraction for the direct photon per-trigger yield. Though the introduction of fiducial cut on π^0 could partially remedy this problem, we still need to consider it by using a fast Monte Carlo simulation.

3.5 Understanding Weighting Function and Fast MC

First, we could write down the detailed statistical equation for $\pi^0 \to$ decay γ,

$$\mathbb{N}^\gamma_{a-b} = \int_a^b dp_T^\gamma \int dz^\gamma \int_0^\infty dp_T^\pi \int dz^\pi \frac{1}{\epsilon_\pi(p_T^\pi, z^\pi)} \cdot P(p_T^\pi, z^\pi, p_T^\gamma, z^\gamma) \cdot \epsilon_\gamma(p_T^\pi, p_T^\gamma, z^\gamma) \cdot \frac{d^2N^\pi(p_T^\pi, z^\pi)}{dp_T^\pi\, dz^\pi} \tag{3.55}$$

Justified by the limited η acceptance of PHENIX central arms, the z distribution of π^0s is flat, then we could get Equation 3.50

$$\mathbb{N}^{\gamma}_{a-b} = \int_a^b dp_T^{\gamma} \int dz^{\gamma} \int_0^{\infty} dp_T^{\pi} \int dz^{\pi} \frac{1}{\epsilon_{\pi}(p_T^{\pi}, z^{\pi})} \cdot P(p_T^{\pi}, z^{\pi}, p_T^{\gamma}, z^{\gamma}) \cdot \epsilon_{\gamma}(p_T^{\pi}, p_T^{\gamma}, z^{\gamma}) \cdot \frac{dN^{\pi}(p_T^{\pi})}{dp_T^{\pi}} \tag{3.56}$$

Note: the flat z distribution of π^0s is important, while the pT distribution of π^0s is not important in the calculation in this section. Actually the z distribution could be any form, only if we could generate π^0 in such a distribution by EXODUS or any other particle generator program.

Notice the variable dependence, as indicated by the different colors,

$$\mathbb{N}^{\gamma}_{a-b} = \int_a^b dp_T^{\gamma} \int dz^{\gamma} \int_0^{\infty} dp_T^{\pi} \int dz^{\pi} \frac{1}{\epsilon_{\pi}(p_T^{\pi}, z^{\pi})} \cdot P(p_T^{\pi}, z^{\pi}, p_T^{\gamma}, z^{\gamma}) \cdot \epsilon_{\gamma}(p_T^{\pi}, p_T^{\gamma}, z^{\gamma}) \cdot \frac{dN^{\pi}(p_T^{\pi})}{dp_T^{\pi}} \tag{3.57}$$

we could integrate z^{π} and z^{γ} at first

$$\mathbb{N}^{\gamma}_{a-b} = \int_a^b dp_T^{\gamma} \int_0^{\infty} dp_T^{\pi} \frac{dN^{\pi}(p_T^{\pi})}{dp_T^{\pi}} \underbrace{\int dz^{\pi} \frac{1}{\epsilon_{\pi}(p_T^{\pi}, z^{\pi})} \cdot \underbrace{\int dz^{\gamma} P(p_T^{\pi}, z^{\pi}, p_T^{\gamma}, z^{\gamma}) \cdot \epsilon_{\gamma}(p_T^{\pi}, p_T^{\gamma}, z^{\gamma})}}_{} \tag{3.58}$$

Now we define the first integral

$$\begin{aligned} g_1(p_T^{\pi}, z^{\pi}, p_T^{\gamma}) &\equiv \int dz^{\gamma} P(p_T^{\pi}, z^{\pi}, p_T^{\gamma}, z^{\gamma}) \, \epsilon_{\gamma}(p_T^{\pi}, p_T^{\gamma}, z^{\gamma}) && (3.59) \\ &\equiv \left[\int dz^{\gamma} P(p_T^{\pi}, z^{\pi}, p_T^{\gamma}, z^{\gamma}) \right] \epsilon_{\gamma}^{*}(p_T^{\pi}, p_T^{\gamma}) && (3.60) \\ &\equiv P^{*}(p_T^{\pi}, z^{\pi}, p_T^{\gamma}) \cdot \epsilon_{\gamma}^{*}(p_T^{\pi}, p_T^{\gamma}) && (3.61) \end{aligned}$$

the two new introduced effective/averaged variables are

$$P^{*}(p_T^{\pi}, z^{\pi}, p_T^{\gamma}) \equiv \int dz^{\gamma} P(p_T^{\pi}, z^{\pi}, p_T^{\gamma}, z^{\gamma}) \tag{3.62}$$

and

$$\epsilon_{\gamma}^{*}(p_T^{\pi}, p_T^{\gamma}) \equiv \frac{\int dz^{\gamma} P(p_T^{\pi}, z^{\pi}, p_T^{\gamma}, z^{\gamma}) \epsilon_{\gamma}(p_T^{\pi}, p_T^{\gamma}, z^{\gamma})}{\int dz^{\gamma} P(p_T^{\pi}, z^{\pi}, p_T^{\gamma}, z^{\gamma})} \tag{3.63}$$

If we make either P or ϵ a constant, it's possible to make it equals with

$$\frac{\int dz^{\gamma} \epsilon_{\gamma}(p_T^{\pi}, p_T^{\gamma}, z^{\gamma})}{\int dz^{\gamma}} \tag{3.64}$$

then we get

$$\mathbb{N}^{\gamma}_{a-b} = \int_a^b dp_T^{\gamma} \int_0^{\infty} dp_T^{\pi} \frac{dN^{\pi}(p_T^{\pi})}{dp_T^{\pi}} \left[\int dz^{\pi} \frac{1}{\epsilon_{\pi}(p_T^{\pi}, z^{\pi})} P^{*}(p_T^{\pi}, z^{\pi}, p_T^{\gamma}) \right] \epsilon_{\gamma}^{*}(p_T^{\pi}, p_T^{\gamma}) \tag{3.65}$$

we define the second integral

$$\begin{aligned} g_2(p_T^{\pi}, p_T^{\gamma}) &\equiv \int dz^{\pi} \frac{1}{\epsilon_{\pi}(p_T^{\pi}, z^{\pi})} P^{*}(p_T^{\pi}, z^{\pi}, p_T^{\gamma}) && (3.66) \\ &\equiv \left[\int dz^{\pi} P^{*}(p_T^{\pi}, z^{\pi}, p_T^{\gamma}) \right] \frac{1}{\epsilon_{\pi}^{\dagger}(p_T^{\pi})} && (3.67) \\ &\equiv P^{\dagger *}(p_T^{\pi}, p_T^{\gamma}) \cdot \frac{1}{\epsilon_{\pi}^{\dagger}(p_T^{\pi})} && (3.68) \end{aligned}$$

the two new introduced effective/averaged variables are

$$P^{\dagger *}(p_T^{\pi}, p_T^{\gamma}) \equiv \int dz^{\pi} P^{*}(p_T^{\pi}, z^{\pi}, p_T^{\gamma}) \tag{3.69}$$

and

$$\epsilon_{\pi}^{\dagger}(p_T^{\pi}) \equiv \frac{\int dz^{\pi} P^{*}(p_T^{\pi}, z^{\pi}, p_T^{\gamma})}{\int dz^{\pi} \frac{1}{\epsilon_{\pi}(p_T^{\pi}, z^{\pi})} P^{*}(p_T^{\pi}, z^{\pi}, p_T^{\gamma})} \tag{3.70}$$

then we get the reduced form of the equation

$$\mathbb{N}_{a-b}^{\gamma} = \int_a^b dp_T^{\gamma} \int_0^{\infty} dp_T^{\pi} \frac{dN^{\pi}(p_T^{\pi})}{dp_T^{\pi}} P^{\dagger *}(p_T^{\pi}, p_T^{\gamma}) \frac{1}{\epsilon_{\pi}^{\dagger}(p_T^{\pi})} \epsilon_{\gamma}^{*}(p_T^{\pi}, p_T^{\gamma}) \tag{3.71}$$

if absorbing the decay photon trigger efficiency into the probability density,

$$W(p_T^{\pi}, p_T^{\gamma}) \equiv P^{\dagger *}(p_T^{\pi}, p_T^{\gamma}) \cdot \epsilon_{\gamma}^{*}(p_T^{\pi}, p_T^{\gamma}) \tag{3.72}$$

The decay photon single particle yield in a finite decay photon pT bin ($a < p_T^{\gamma} < b$) is

$$\mathbb{N}_{a-b}^{\gamma} = \int_a^b dp_T^{\gamma} \int_0^{\infty} dp_T^{\pi} \frac{dN^{\pi}(p_T^{\pi})}{dp_T^{\pi}} W(p_T^{\pi}, p_T^{\gamma}) \frac{1}{\epsilon_{\pi}^{\dagger}(p_T^{\pi})} \tag{3.73}$$

Integrated by p_T^{γ}

$$\mathbb{N}_{a-b}^{\gamma} = \int_0^{\infty} dp_T^{\pi} \frac{dN^{\pi}(p_T^{\pi})}{dp_T^{\pi}} W_{a-b}^{\star}(p_T^{\pi}) \frac{1}{\epsilon_{\pi}^{\dagger}(p_T^{\pi})} \tag{3.74}$$

here

$$W_{a-b}^{\star}(p_T^{\pi}) \equiv \int_a^b dp_T^{\gamma} W(p_T^{\pi}, p_T^{\gamma}) \tag{3.75}$$

The discrete form of Equation 3.74 is

$$\mathbb{N}_{a-b}^{\gamma} = \sum_{i=1}^{N^{\pi}} \frac{W_{a-b}^{\star}(p_T^{\pi_i})}{\epsilon_{\pi}^{\dagger}(p_T^{\pi_i})} \tag{3.76}$$

Similarly, if ignoring the charged track efficiency(could be factored out), the decay γ-h pair yield in a finite trigger pT bin ($a < p_T^{\gamma} < b$) is

$$\mathbb{N}_{a-b}^{\gamma-h} = \int_a^b dp_T^{\gamma} \int_0^{\infty} dp_T^{\pi} \frac{dN^{\pi-h}(p_T^{\pi})}{dp_T^{\pi}} W(p_T^{\pi}, p_T^{\gamma}) \frac{1}{\epsilon_{\pi}^{\dagger}(p_T^{\pi})} \tag{3.77}$$

$$= \int_0^{\infty} dp_T^{\pi} \frac{dN^{\pi-h}(p_T^{\pi})}{dp_T^{\pi}} W_{a-b}^{\star}(p_T^{\pi}) \frac{1}{\epsilon_{\pi}^{\dagger}(p_T^{\pi})} \tag{3.78}$$

and its discrete form

$$\mathbb{N}_{a-b}^{\gamma-h} = \sum_{i=1}^{N^{\pi}} \sum_{j=1}^{M_{\pi_i}^{h}} \frac{W_{a-b}^{\star}(p_T^{\pi_i})}{\epsilon_{\pi}^{\dagger}(p_T^{\pi_i})} \tag{3.79}$$

$$= \sum_{i=1}^{N^{\pi}} M_{\pi_i}^{h} \cdot \frac{W_{a-b}^{\star}(p_T^{\pi_i})}{\epsilon_{\pi}^{\dagger}(p_T^{\pi_i})} \tag{3.80}$$

where $M_{\pi_i}^{h}$ is the number of hadron partners associated with i-th π^0 trigger.

In the final, we could express the two-particle correlaton per-trigger yield for decay photon triggers

$$PTY_{decay} = \frac{\sum_{i=1}^{N^{\pi}} M_{\pi_i}^{h} \cdot W_{a-b}^{\star}(p_T^{\pi_i}) / \epsilon_{\pi}^{\dagger}(p_T^{\pi_i})}{\sum_{i=1}^{N^{\pi}} W_{a-b}^{\star}(p_T^{\pi_i}) / \epsilon_{\pi}^{\dagger}(p_T^{\pi_i})} \tag{3.81}$$

Equation 3.81 is my derived version of Equation 3.54 from the reference [20]. Although the π^0 trigger efficiency can not cancel out here, the absolute normalization factor in deed could be cancel out, which is clearly shown in the equation 3.81 above.

In practice, the procedure to remove the z dependence and ϵ_γ, as shown in the mathematical steps above, is performed by fast Monte Carlo simulation.

By the way, the single particle efficiency for the decay photons is $\epsilon_\gamma(p_T^\pi, p_T^\gamma, z^\gamma)$, which depends on the parent π^0's pT value. This dependence comes from two effects. One is the merging effect of two photon in EMCal. If the parent π^0's pT is high enough(above 12 GeV/c), the two daughter decay photons could merge together, and rejected by the shower-shape veto. The other results from the charge track and photon distance veto. The opening angle between two nearby high pT π^0s is small, if one of them decay by the Dalitz decay channel $\pi^0 \to \gamma + e^- + e^+$ (about 1.2% probability), the daughter photons from the other π^0 could be rejected by the charge track and photon distance veto. The distance between two high pT π^0s tends to be smaller than low pT π^0s.

3.6 Isolation Cut

Though statistical subtraction method proves a reliable technique in two-particle jet correlation, the application of the isolation cut could enhance the direct photon signal and increase the statistics. The main idea of the isolation cut is that the scattering prompt photon and the parton are in nearly opposite directions such that there are few particles in the jet fragmented from the parton around the prompt photon or we could say that the prompt photon is isolated. However, this idea is complicated by the underlying events, of which soft components could contaminate the isolated situation of the direct photon. And the direct photons which come from the fragmentation directly are also accompanied by the hadrons from the fragmentation process.

In this analysis, the isolated triggers, including the phones and the π^0s which are the parent of the decay photons, should satisfy these requirements:

- Sum Rule: The sum of the energy of photons and pT of charged particles within a cone of 0.3 should be less than 10% of the energy of the trigger. Here, the distance of the i-th particle and the trigger is represented by $\sqrt{(\phi_{trig} - \phi_i)^2 + (\eta_{trig} - \eta_i)^2}$, which should be less than the cone size 0.3.
- Fiducial Cut: The trigger should not be on the edge of EMCal to prevent the cone is partly outside of the acceptance coverage, which is not applied currently.

Similarly, the direct photon yield in the isolation cut method is extracted by subtracting the decay photon yield from the inclusive one. However, due to the enhancement of the direct photon signal, the value of R_γ is much greater than that without the isolation cut. Actually, R_γ^{iso} should be redefined as

$$R_\gamma^{iso} \equiv \frac{N_{inc}^{\gamma,iso}}{N_{dec}^{\gamma,iso}} \tag{3.82}$$

The inclusive isolated photons could be obtained very easily, while the isolated decay photons should be treated carefully. We could map the π^0s without isolation cut applied to the decay photons by the fast Monte Carlo simulation, then apply the isolation cut and count the isolated decay photons which still remain there. In the end, the modification of R_γ^{iso} would make the direct photon sample much similar to the inclusive one.

Chapter 4

Current Progress

The two-particle correlation per-trigger yields for the centrality 0-20%, 20-40%, 40-60%, 60-80%, 0-88% are obtained with various pT bins of triggers and associate hadrons. The p_T bins of triggers are 5-7 GeV/c, 7-9 GeV/c, 9-12 GeV/c, 5-10 GeV/c, 12-15 GeV/c respectively, and the p_T bins of associate hadrons are 1-2 GeV/c, 2-3 GeV/c, 3-5 GeV/c, 5-10 GeV/c respectively. They are shown in the following sections.

4.1 π^0 Trigger Efficiency

As discussed in Section 3.5, the π^0 trigger efficiency is essential for us to obtain the decay (and therefore the direct photon) per-trigger yields, which could be seen very clearly in Equation 3.81. Though the absolute value of the π^0 trigger efficiency doesn't matter, the shape is very critical for a proper statistical subtraction to get the direct photon result.

The π^0 trigger efficiencies for all centrality bins are obtained by comparing the single π^0 raw yield with the published PHENIX data [21]. The π^0 trigger efficiency for the centrality bin 0-20% is shown in Figure 4.1. The dramatic efficiency loss in the high p_T region ($p_T > 12$ GeV) results from the merging effect as discussed in Section 3.3. The reason for low efficiency in p_T range 4-7 GeV is the asymmetry cut applied in this analysis, which could affect the efficiency when π^0 energy goes below 5.25 GeV. FYI, the asymmetry cut formula is:

$$\frac{\Delta E}{E_{sum}} < 0.15 + 0.85 \times \left(\frac{E_{sum} - 4}{1.25}\right)^2 \tag{4.1}$$

This cut removes background in very high multiplicity events, but may be removed for in the future.

4.2 Two-Particle Correlation by Statistical Subtraction

As shown in Equation 3.81, with the weighting function and the π^0 trigger efficiency determined, the per-trigger yield correlation function could be obtained for the decay photon case. Then this can be subtracted from the inclusive photon result, yielding the final two-particle correlation per-trigger yield for direct photon from statistical subtraction. The inclusive γ-h, π^0-h, decay γ-h, and the direct γ-h pair correlation per-trigger yields are shown in Figure 4.2, 4.3, 4.4, 4.5 respectively.

As we can see, in some high pT bins, the two-particle correlation per trigger yields lack the statistics compared with the lower pT bins. The single particle yields, both the triggers and the partners, decrease dramatically when their pT value increase. In turn, the two-particle pair yields get rare accordingly. This

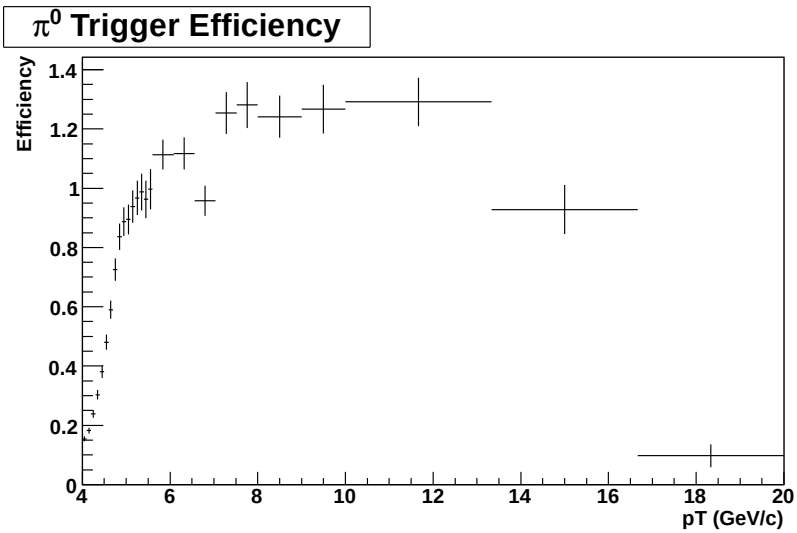

Figure 4.1: π^0 trigger efficiency for the centrality bin 0-20%. X-axis is π^0's pT value in GeV/c, and Y-axis is the π^0 trigger efficiency. It's normalized by an arbitrary factor which could be cancel out in our precedure, see Equation 3.81.

phenomena is notable especially in the central region $\Delta\phi \approx \pi/2$ where very few of near- or away-side jet components resides.

Another problem is that the statistical fluctuation in the direct photon's plots is remarkable. This results from the samll signal/background ratio. The direct photons are very rare compared with the decay photons, which could be found almost in every event with a large multiplicity. To address this issue, we also apply the isolation cut on the triggers, both on the photons and the π^0s. Because the direct photons, especially the prompt photons from the Compton process, are expected to be isolated and associated with no jet components nearby. Also, this isolation requirement could help to reduce the fraction of fragmentation photons in the direct photon sample. The results are presented in the next section.

4.3 Two-Particle Correlation with Isolation Cut

To enhance the s/b ratio in the inclusive photon sample, the isolation cut is applied on the triggers, both on the photons and the π^0s. It requires that the sum of charged hadrons' momenta and photons' energy inside a cone with size about 0.3 should be less than 10% of the trigger's energy. Because the PHENIX central arms cover 0.7 in pseudorapidity, which is comparable to the cone size, some of the cone area is outside of the detector acceptance. To ameliorate this issue, fiducial cuts are applied on the triggers, which requires that the trigger, no matter a photon or a π^0, should not locate near the detector edges by 0.1, both in η and ϕ. This could make the effective acceptance for photons and π^0s much more similar.

The two-particle correlation per-trigger yields have been obtained with the isolation cut applied, shown in Figure 4.6, 4.7, 4.8 respectively, except for the direct photon, because the value of R_γ still needs to be determined. As shown in the plots, the near-side yields are greatly suppressed which is the result of the isolation cut, furthermore, the away-side yields are greatly enhanced which benefits from the much larger signal/background ratio in the isolation cut study.

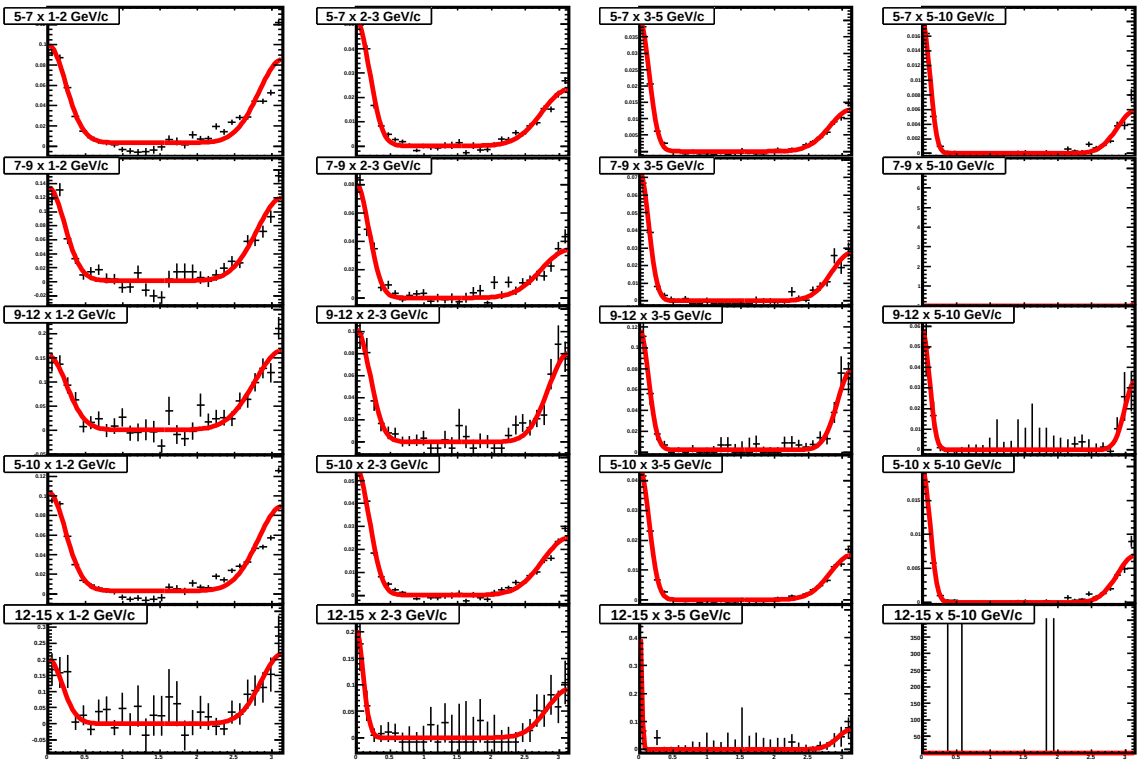

Figure 4.2: The inclusive γ-h correlation function per-trigger yields for centrality 0-88% are shown for various pT bins for the triggers and the associate partners. The X-axis is $\Delta\phi$, from 0 to 2π. The Y-axis is the per-trigger yields, defined as $\frac{1}{N_{trig}}\frac{dN}{d\Delta\phi}$. From top to bottom, the trigger pT bins are 5-7 GeV/c, 7-9 GeV/c, 9-12 GeV/c, 5-10 GeV/c, 12-15 GeV/c. From left to right, the parner pT bins are 1-2 GeV/c, 2-3 GeV/c, 3-5 GeV/c, 5-10 GeV/c. The red lines are fitted by near- and away-side Gaussian peaks.

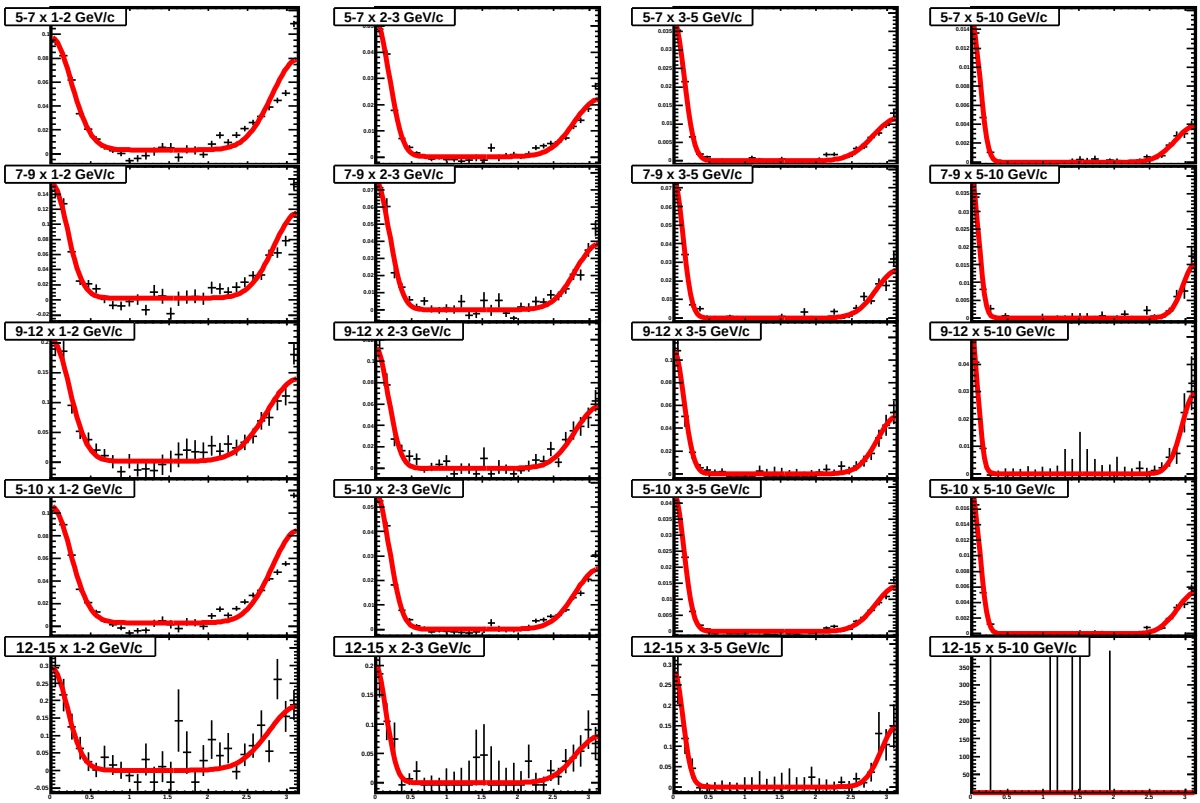

Figure 4.3: π^0-h correlation function per-trigger yields for centrality 0-88% are shown for various pT bins for the triggers and the associate partners. The X-axis is $\Delta\phi$, from 0 to 2π. The Y-axis is the per-trigger yields, defined as $\frac{1}{N_{trig}}\frac{dN}{d\Delta\phi}$. From top to bottom, the trigger pT bins are 5-7 GeV/c, 7-9 GeV/c, 9-12 GeV/c, 5-10 GeV/c, 12-15 GeV/c. From left to right, the parner pT bins are 1-2 GeV/c, 2-3 GeV/c, 3-5 GeV/c, 5-10 GeV/c. The red lines are fitted by near- and away-side Gaussian peaks.

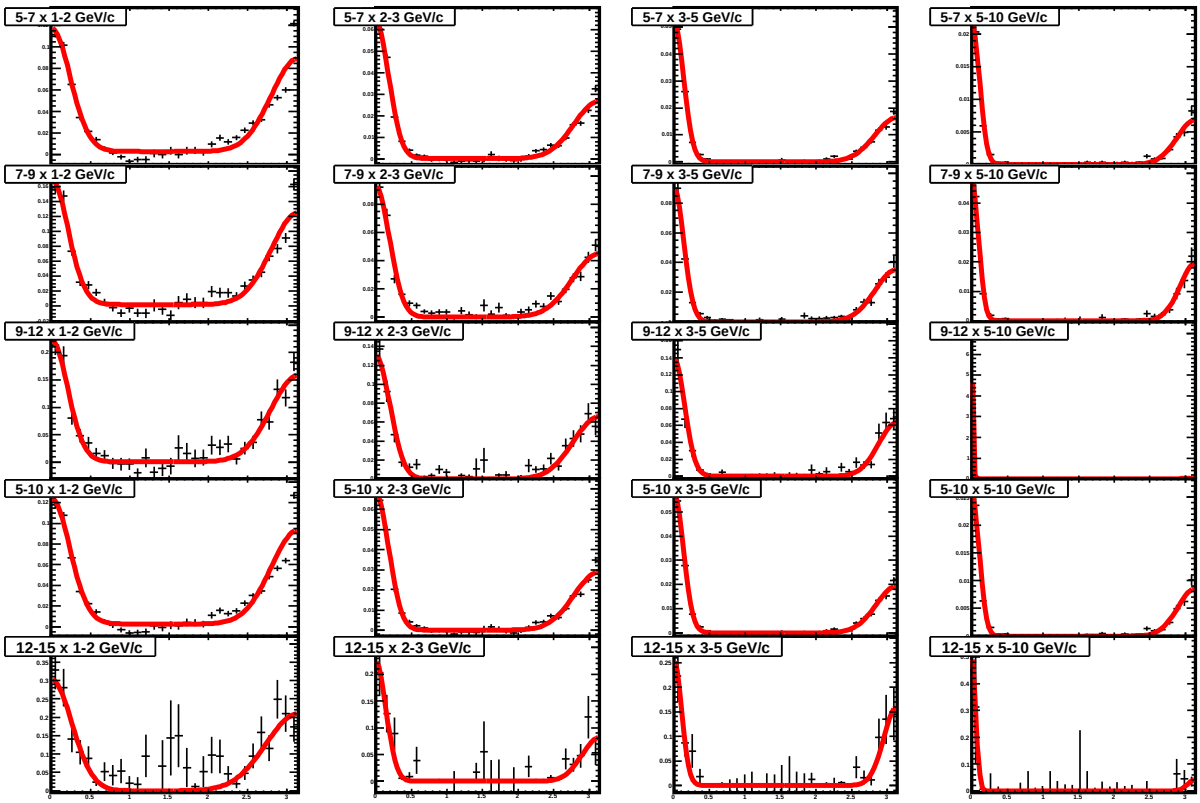

Figure 4.4: The decay γ-h correlation function per-trigger yields for centrality 0-88% are shown for various pT bins for the triggers and the associate partners. The X-axis is $\Delta\phi$, from 0 to 2π. The Y-axis is the per-trigger yields, defined as $\frac{1}{N_{trig}}\frac{dN}{d\Delta\phi}$. From top to bottom, the trigger pT bins are 5-7 GeV/c, 7-9 GeV/c, 9-12 GeV/c, 5-10 GeV/c, 12-15 GeV/c. From left to right, the parner pT bins are 1-2 GeV/c, 2-3 GeV/c, 3-5 GeV/c, 5-10 GeV/c. The red lines are fitted by near- and away-side Gaussian peaks.

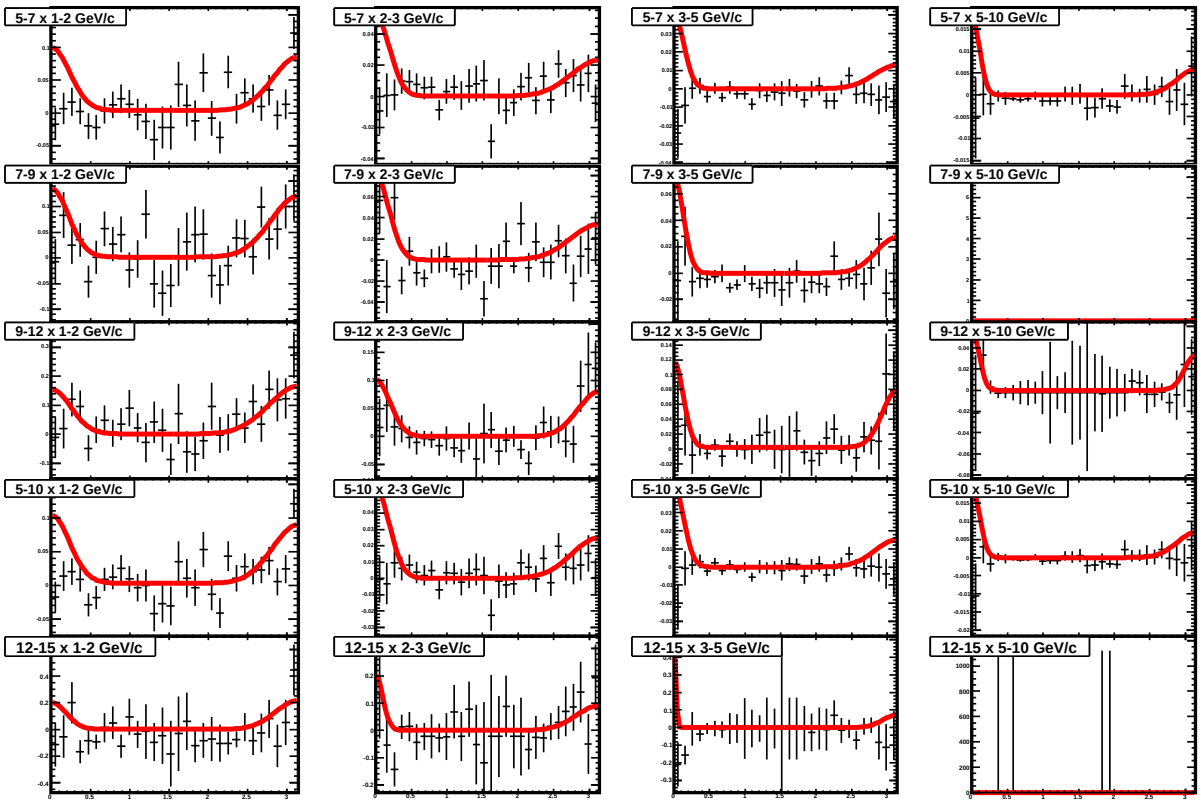

Figure 4.5: The direct γ-h correlation function per-trigger yields for centrality 0-88% are shown for various pT bins for the triggers and the associate partners. The X-axis is $\Delta\phi$, from 0 to 2π. The Y-axis is the per-trigger yields, defined as $\frac{1}{N_{trig}}\frac{dN}{d\Delta\phi}$. From top to bottom, the trigger pT bins are 5-7 GeV/c, 7-9 GeV/c, 9-12 GeV/c, 5-10 GeV/c, 12-15 GeV/c. From left to right, the parner pT bins are 1-2 GeV/c, 2-3 GeV/c, 3-5 GeV/c, 5-10 GeV/c. The red lines are fitted by near- and away-side Gaussian peaks.

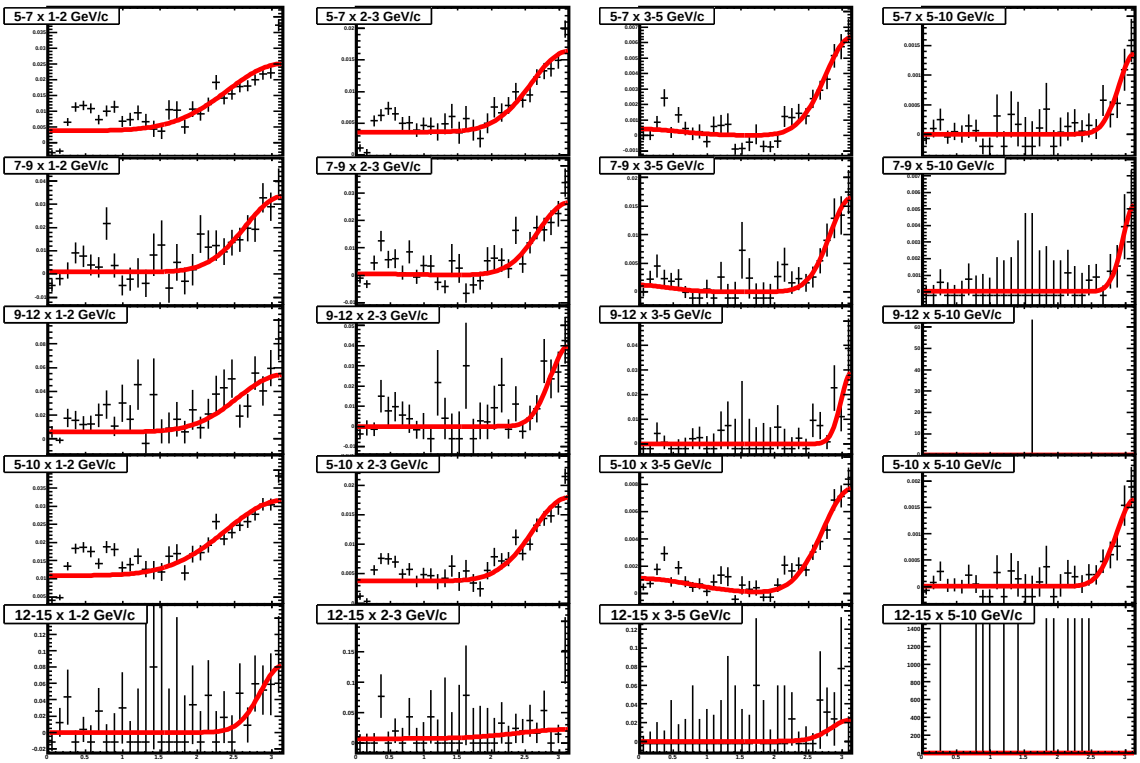

Figure 4.6: The inclusive γ-h correlation function per-trigger yields for centrality 0-88% with isolation cut are shown for various pT bins for the triggers and the associate partners. The X-axis is $\Delta\phi$, from 0 to 2π. The Y-axis is the per-trigger yields, defined as $\frac{1}{N_{trig}}\frac{dN}{d\Delta\phi}$. From top to bottom, the trigger pT bins are 5-7 GeV/c, 7-9 GeV/c, 9-12 GeV/c, 5-10 GeV/c, 12-15 GeV/c. From left to right, the parner pT bins are 1-2 GeV/c, 2-3 GeV/c, 3-5 GeV/c, 5-10 GeV/c. The red lines are fitted by near- and away-side Gaussian peaks.

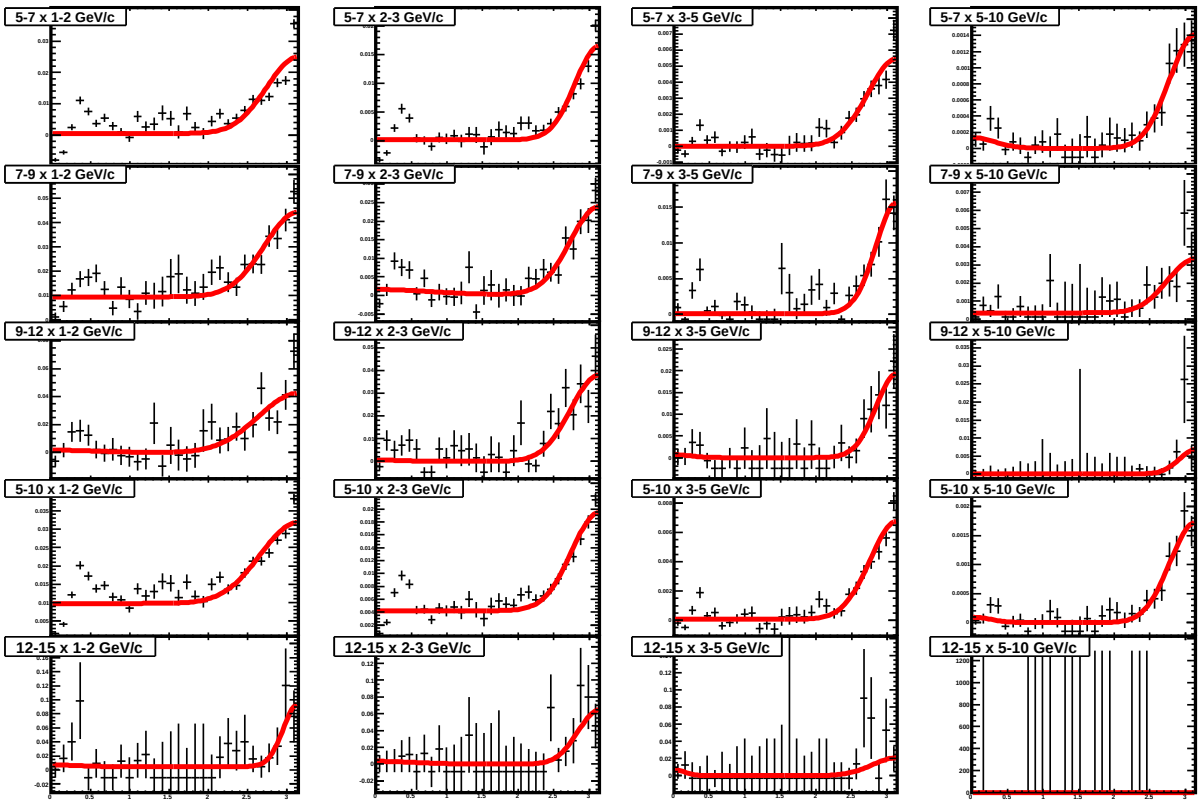

Figure 4.7: π^0-h correlation function per-trigger yields for centrality 0-88% with isolation cut are shown for various pT bins for the triggers and the associate partners. The X-axis is $\Delta\phi$, from 0 to 2π. The Y-axis is the per-trigger yields, defined as $\frac{1}{N_{trig}}\frac{dN}{d\Delta\phi}$. From top to bottom, the trigger pT bins are 5-7 GeV/c, 7-9 GeV/c, 9-12 GeV/c, 5-10 GeV/c, 12-15 GeV/c. From left to right, the parner pT bins are 1-2 GeV/c, 2-3 GeV/c, 3-5 GeV/c, 5-10 GeV/c. The red lines are fitted by near- and away-side Gaussian peaks.

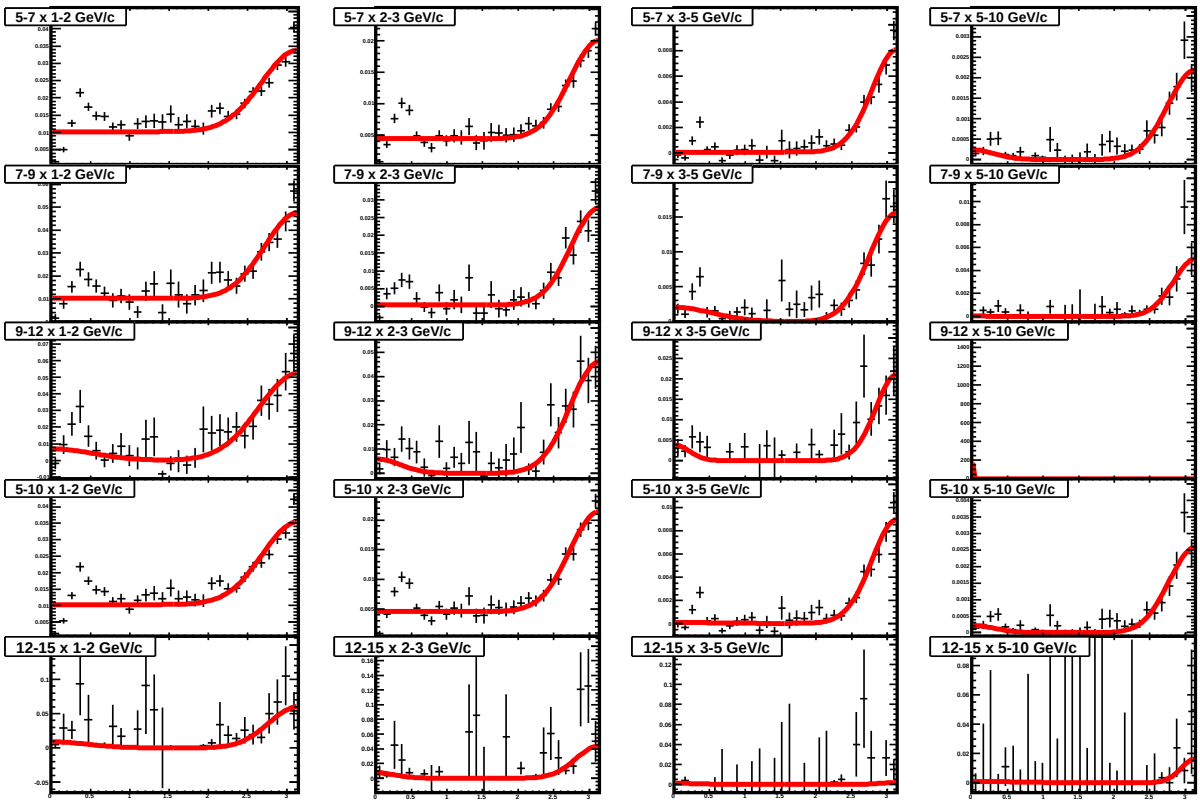

Figure 4.8: The decay γ-h correlation function per-trigger yields for centrality 0-88% with isolation cut are shown for various pT bins for the triggers and the associate partners. The X-axis is $\Delta\phi$, from 0 to 2π. The Y-axis is the per-trigger yields, defined as $\frac{1}{N_{trig}}\frac{dN}{d\Delta\phi}$. From top to bottom, the trigger pT bins are 5-7 GeV/c, 7-9 GeV/c, 9-12 GeV/c, 5-10 GeV/c, 12-15 GeV/c. From left to right, the parner pT bins are 1-2 GeV/c, 2-3 GeV/c, 3-5 GeV/c, 5-10 GeV/c. The red lines are fitted by near- and away-side Gaussian peaks.

Chapter 5

Future Plan

5.1 Plan

The initial results have been obtained for the γ-h azimuthal correlations in d+Au collisions, including the correlation function from statistical subtraction and the isolation cut method. To achieve our goals mentioned in Chapter 1, some kinematic variables should be measured in the next step. To observe the k_T effect, we could use the quantity $\hat{x}_h$, which is the ratio of the two outgoing jet momentum $p_T^{away_jet}/p_T^{trigger_jet_\gamma}$, to measure the transverse momentum imbalance between the trigger and associated partons. The value is one in the leading order, but could deviate from unity due to the k_T effect. In the other hand, we could measure the momentum of jet products in the direction orthogonal to the parton pair direction. Any deviation from zero shows the effect other than the leading order and the k_T effect. $\vec{p}_{out}$ represents the acoplanary which related to the p_T imbalance. Actually, the acoplanary is essentially equivalent to the p_T imbalance, just that in some other axis which is a combination of x-, y-, z-axes. This quantity are defined as

$$|\vec{p}_{out}| = |p_T^{assoc}| \sin \Delta\phi \tag{5.1}$$

Other important quantities which we would like to measure are

$$x_E = -\frac{\vec{p}_T^{trig} \cdot \vec{p}_T^{assoc}}{|p_T^{trig}|^2} = -\frac{|p_T^{assoc}|}{|p_T^{trig}|} \cos \Delta\phi \tag{5.2}$$

If $p_T^{trig} \approx \hat{p}_T^{trig}$, the x_E distribution approximates the fragmentation function $D(z)$, where $z = \frac{E_h}{E_{parton}}$. This is valid for direct photon in the leading order. Sometime, another quantity z_T equivalent to x_E could be used,

$$z_T = \frac{p_T^{assoc}}{p_T^{trig}} \tag{5.3}$$

where in the above formula now "trigger" and "associated" refer to the two particles in the two-particle correlation, not the two parent jets, except when one of them is actually a direct photon.

Therefore, by studying the dependence of the yields on the transverse momentum of the trigger and the associated hadrons, we could plot the yields as a function of z_T or x_E, which would then approximate the fragmentation function. In practice, the plots for the distribution of these jet kinematic variables, such as yield-x_E, yield-z_T, yield-p_{out} plots, are binned for these variables. Accordingly, such plots can simply be obtained by integrating the away-side $dN/d\delta\phi(\phi > \pi/2)$ yields in the correlation function of a certain choice of trigger and partner pT bins. Also, these kind of plots could lead to a comparison between the shapes

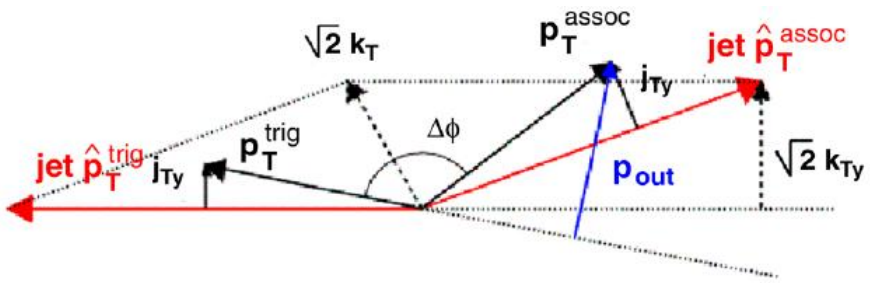

Figure 5.1: A diagram from [22] showing the jet dynamics variables. Two momentum $\hat{p}_T^{trig}$ and $\hat{p}_T^{assoc}$ denote the transverse momentum of the hard scattered parton/direct photon. $\vec{p}_T^{trig}$ and $\vec{p}_T^{assoc}$ are the transverse momentum of the trigger and associated hadron respectively. $\vec{p}_{out}$ is defined as a vector transverse to $\vec{p}_T^{trig}$.

of p+p, Au+Au and d+Au plots and indicate possible modifications. The p+p and Au+Au results have been measured already, see Figure 5.2 (from PHENIX), so our measurement could clearly show the possible modification in d+Au collision, and present the cold nuclear effect on the jet fragmentation and see how it contributes to the modification seen in Au+Au collision.

In summary, we could perform the measurements in the list

- the per-trigger yield, compare with the value in p+p, get the ratio, namely I_{dA}, to furthe study the modification with enhanced precesion (by the direct photon trigger)
- p_{out} distribution, plot the yields in bins of p_{out} and fit the away-side correlation function, get $\sqrt{\langle |p_{out}|^2 \rangle}$ from the away-side peak width to evaluate the acoplanary (i.e. k_T effect in d+Au)
- x_E distribution, plot the yield as a function of x_E(in bins), measure the modification of jet fragmentation
- by selecting or expanding the types of hadrons in the associated particles, we could pursue other ideas discussed in Section 5.2.

5.2 Outlook

In addition to the plan in Section 5.1, the following measurements will be done, all of which will be he first time at RHIC:

- Charge sign separation in the associated particles: By measuring the positive and negative hadrons separately, the ratio of the per-trigger yields for γ-h^+ and $\gamma - h^-$, as shown in Figure 1.3, could be obtained. This will verify that the deviation of this ratio from di-jet result in p+p is due to the expected quark dominance in $\gamma - h$ correlation by changing the ratio of u, d quarks. All the required methods, such as the direct photon id and the combinatorics subtraction, are the same as current analysis. A similar plot for p+p collision is shown in figure 5.3.
- Baryon / meson separation in the associated aprtices: By using the time of flight to EMCal, PHENIX is able to separate baryon or meson parters. Comparing the ratio of the yields of the two particle types with di-jet result, we could possibly see that the gluon jets have higher probability to fragment into baryons than quark jets. All the required methods are the same as current analysis.

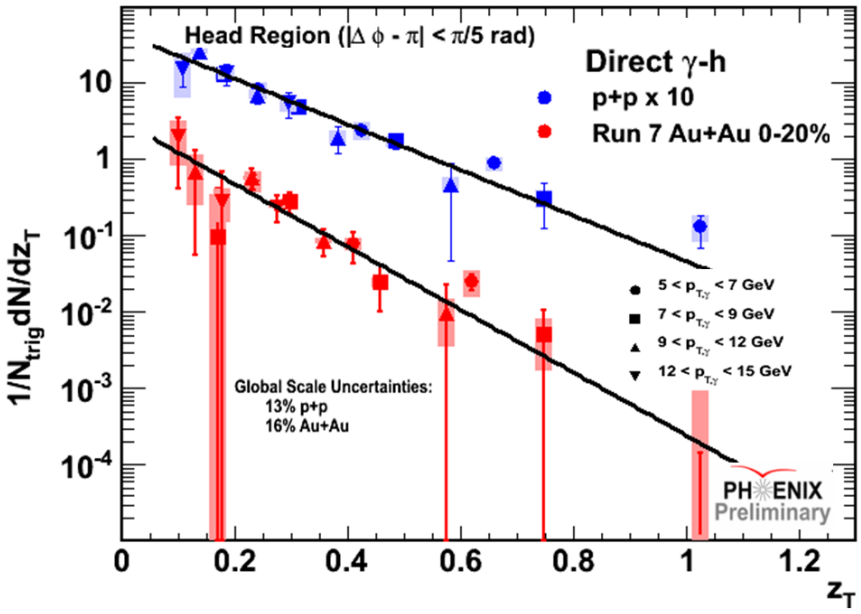

Figure 5.2: z_T distribution in p+p and Au+Au collision. The solid lines are fitted universally for all jet energy. The p+p slope is 6.89 ± 0.64, while the Au+Au slope is 9.49 ± 1.37. The Au+Au slope is about $\sim 1.3\sigma$ higher than p+p.

- Use π^0 measureded in MPC in the forward region as the associated partners to test the gluon saturation phenomena which is described in Chapter 1. It is pretty straightforward to change the associated particles from the central arm tracks to the π^0s (reconstructed from decay photons deteced by MPC) in the forward region. The systematics associated with the direct photon identification (statistical subtraction, isolation cut) are the same as the current analysis. The code to include MPC particles has alredy been developed, so the only additional work is to optimize MPC cuts (some have already been done by other PHENIX collaborators stuying MPC yields). Similar work is undergoing for mid/forward-rapidity π^0/π^0 correlations in d+Au collisions [11]. The correlation function per-trigger yield in d+Au collision is substantially suppressed, as shown in Figure 5.4. The triggers in this work is the π^0 reconstructed from decay photons detected by EMCal in the midrapidity. My work would change the triggers from π^0 to direct photon in midrapidity.

5.3 Unfinished Work

Before going to extract any data for publish, some things left over should be done, including:

- associated particle efficiency, the yields need to be corrected for the associated hadron lost due the detect effeciency. This could be done either by the simulation or by comparing the raw yields with published data

- R_γ determination, To properly subtract the decay photon contribution, R_γ is an essential parameter. However it's an input parameter for our analysis. Currently, R_γ is being studied in the analysis of the single photon spectra / corss-section by other PHENIX collaborators, which would be done within a few months and well before our result is ready for publish.

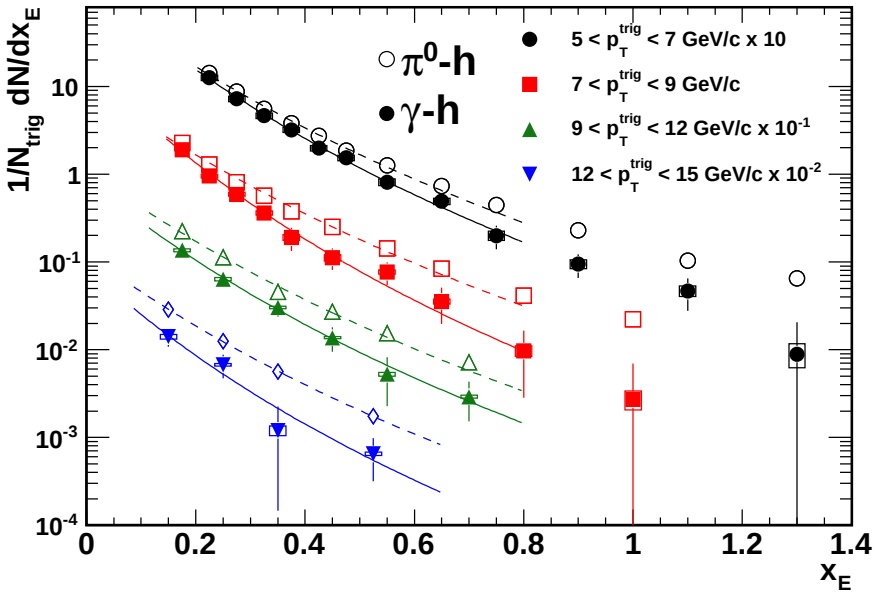

Figure 5.3: Away-side yield as a function of x_E in p+p collision [7]. The solid lines are fitted from the modified Hagedorn function.

- absolute normalization for background subtraction, discussed in Section 3.3.3, this is an alternative for the method used our analysis, which help to evaluate the systematic uncertainty associated with the two-source model assumption
- η meson correction, discussed in Section 3.2.2, the per-trigger yield for η meson trigger would be studied as well, and η contribution to decay photon should be subtracted from the inclusive photon.

5.4 Possible Work

If time permitted, I would like to apply the isolation cut in Au+Au collisions, at least in peripheral collisions, which would be interesting. The isolation cut has long been applied in the direct photon measurements in hadron colliders with various energy from 630 GeV to 1.8 TeV by UA2 [23], D0 [24] [25] and CDF [26] [27] [28]. The performance of the isolation cut in such a high multiplicity environment in RHIC Au+Au collision at 200 GeV is yet to evaluated. The jet kinematics should be studied with a certain sized cone and the proper parameter for this isolation cut should be tuned in order to maximally enhance the direct photon signal, or say, remove the underlying events and the decay products. In this way, a direct comparison between Au+Au and d+Au results could be established, and the evidence to discriminate the cold and hot nuclear effect could be observed, which in the final would help to make a firm ground for the QGP signature claimed by the previous Au+Au measurements on RHIC data. This plan depends on my work progress and the results from the first stage, such as the statistical limit and the systematic uncertainty.

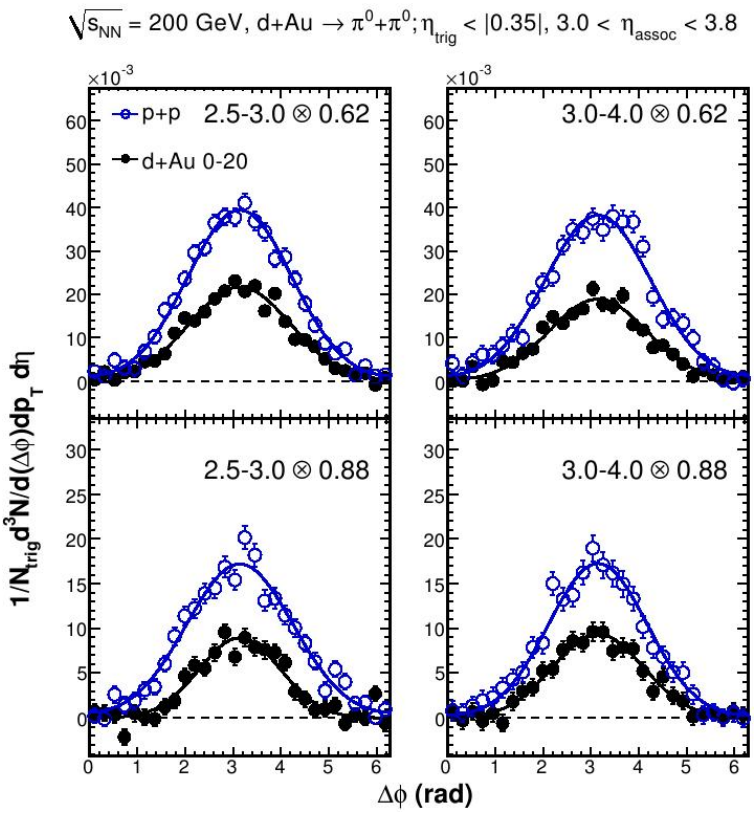

Figure 5.4: Midrapidity / forward rapidity π^0 / π^0 correlation function per-trigger yield in p+p and central and peripheral d+Au collision [11]. The d+Au result is found to be substantially suppressed.

Chapter 6

Notes

6.1 Decay Photon Boost

In the lab frame, we take the direction of the parent π^0 as the x-axis, and y-,z-axises are chosen radomly. The π^0 rest frame keeps the same axis, but it is boosted by π^0 velocity. In the same way, we could deem the lab frame is boosted by the π^0 rest frame in the opposite direction. Therefore, $\beta = \beta'$ and $\gamma = \gamma'$ for the Lorentz transfromation between the two frames. We could write down the detailed Lorentz transformation from the π^0 rest frame to the lab frame,

$$\begin{pmatrix} E \\ p_x \\ p_y \\ p_z \end{pmatrix} = \begin{pmatrix} \gamma & \beta\gamma & 0 & 0 \\ \beta\gamma & \gamma & 0 & 0 \\ 0 & 0 & 1 & 0 \\ 0 & 0 & 0 & 1 \end{pmatrix} \begin{pmatrix} E' \\ p'_x \\ p'_y \\ p'_z \end{pmatrix} \tag{6.1}$$

If we let the angle between one daughter photon and the parent π^0 (actually, π^0 is still in its own frame, but we take its track in the lab frame as x axis both in the lab frame and the π^0 rest frame) in the π^0 rest frame is Ψ (It's safe for us to assume that $0 \leq \Psi \leq \pi/2$ and both $\cos\Psi$ and $\sin\Psi \geq 0$)

$$E' = \frac{m_\pi}{2} \tag{6.2}$$

$$p'_x = \frac{m_\pi}{2}\cos\Psi \tag{6.3}$$

$$p'_y = \frac{m_\pi}{2}\sin\Psi\cos\Phi \tag{6.4}$$

$$p'_z = \frac{m_\pi}{2}\sin\Psi\sin\Phi \tag{6.5}$$

then

$$\begin{pmatrix} E \\ p_x \\ p_y \\ p_z \end{pmatrix} = \begin{pmatrix} \gamma & \beta\gamma & 0 & 0 \\ \beta\gamma & \gamma & 0 & 0 \\ 0 & 0 & 1 & 0 \\ 0 & 0 & 0 & 1 \end{pmatrix} \cdot \frac{m_\pi}{2} \cdot \begin{pmatrix} 1 \\ \cos\Psi \\ \sin\Psi\cos\Phi \\ \sin\Psi\sin\Phi \end{pmatrix} \tag{6.6}$$

We get the four momentum of the first daughter photon in the boosted lab frame

$$\begin{pmatrix} E_1 \\ p_{x,1} \\ p_{y,1} \\ p_{z,1} \end{pmatrix} = \begin{pmatrix} \gamma + \beta\gamma\cos\Psi \\ \beta\gamma + \gamma\cos\Psi \\ \sin\Psi\cos\Phi \\ \sin\Psi\sin\Phi \end{pmatrix} \tag{6.7}$$

The other photon could be denoted by change $\Psi \to \pi - \Psi$ and $\Phi \to \Phi + \pi$

$$\begin{pmatrix} E_2 \\ p_{x,2} \\ p_{y,2} \\ p_{z,2} \end{pmatrix} = \begin{pmatrix} \gamma - \beta\gamma\cos\Psi \\ \beta\gamma - \gamma\cos\Psi \\ -\sin\Psi\cos\Phi \\ -\sin\Psi\sin\Phi \end{pmatrix} \tag{6.8}$$

If we use Ω to denote the angle between the daughter photon and the parent π^0 in the lab frame, they should be

$$\tan\Omega_1 = \frac{|\sin\Psi|}{\beta\gamma + \gamma\cos\Psi} = \frac{\sin\Psi}{\beta\gamma + \gamma\cos\Psi} \tag{6.9}$$

$$\tan\Omega_2 = \frac{|\sin\Psi|}{\beta\gamma - \gamma\cos\Psi} = \frac{\sin\Psi}{\beta\gamma - \gamma\cos\Psi} \tag{6.10}$$

Then the angle Ω between the two daughter photons boosted in the lab frame is

$$\tan\Omega = \tan(\Omega_1 + \Omega_2) \tag{6.11}$$

$$= \frac{\tan\Omega_1 + \tan\Omega_2}{1 - \tan\Omega_1 \cdot \tan\Omega_2} \tag{6.12}$$

$$= \frac{2\beta\gamma\sin\Psi}{\gamma^2(\beta^2 - \cos^2\Psi) - \sin^2\Psi} \tag{6.13}$$

Because

$$E_1 = \gamma + \beta\gamma\cos\Psi \tag{6.14}$$

$$E_2 = \gamma - \beta\gamma\cos\Psi \tag{6.15}$$

we get the energy asymmetry α in the lab frame

$$\alpha = \frac{\Delta E}{E_1 + E_2} = \frac{|2\beta\gamma\cos\Psi|}{2\gamma} = \beta\cos\Psi \tag{6.16}$$

here, we can see that $\alpha \uparrow \Rightarrow \cos\Psi \uparrow \Rightarrow \Psi \downarrow$ in the π^0 rest frame. Also, we can get the range of α in the lab frame is $[0, \beta]$ because of Lorentz boost limitation (the two daughters always have same energy in the π^0 rest frame). In the lab frame, the decay pair angle is

$$\tan\Omega = \frac{2\beta\gamma\sqrt{1 - \alpha^2/\beta^2}}{\gamma^2(\beta^2 - \alpha^2/\beta^2) - (1 - \alpha^2/\beta^2)} \tag{6.17}$$

If we substitude $\sqrt{1 - \alpha^2/\beta^2}$ by t, then

$$\tan\Omega = \frac{2\beta\gamma t}{\gamma^2(\beta^2 - 1 + t^2) - t^2} \tag{6.18}$$

If we assume the pT or E of the parent π^0 is about 10GeV, then $\gamma = \frac{E}{m_\pi} \sim 50$, and $\beta \sim 1 - \Delta$ (here Δ is a small number), and the range for α is $0 \leq \alpha \leq \cos\Psi$, then

Bibliography

[1] http://en.wikipedia.org/wiki/Quark 6

[2] K. Adcox et al. (PHENIX Collaboration), Phys. Rev. Lett. **88**, 022301 (2002). 6

[3] S. S. Adler et al. (PHENIX Collaboration), Phy. Rev. Lett **91**, 072303 (2003). 6

[4] S. S. Adler et al. (PHENIX Collaboration), Phy. Rev. C **73**, 054903 (2006). 7

[5] R. P. Feynman et al , Nucl. Phy. B bf128, 1-65 (1977). 7

[6] L. Apanasevich et al. Phy. Rev. D **59**, 074007 (1999). 7

[7] A. Adare et al. (PHENIX Collaboration), Phys. Rev. D **82**, 072001 (2010). 7, 8, 9, 50

[8] C. Adler et al. (STAR Collaboration), Phy. Rev. Lett. **90**, 082302 (2003). 7

[9] A. Adare et al. (PHENIX Collaboration), Phy. Rev. C **78**, 014901 (2008). 7, 31

[10] I. Arsene et al. (BRAHMS Collaboration), Phy. Rev. Lett. **93**, 242303 (2004). 8

[11] B. Meredith et al. (PHENIX Collaboration), PPG 128 within PHENIX 8, 9, 49, 51

[12] Larry Mclerran and Raju Venugopalan, Phy. Rev. D **49**, 3352 (1994). 8

[13] Dmitri Kharzeev, Eugene Levin, and Larry McLerran. Nucl. Phys., A **78** 627 (2005). 9

[14] M. L. Miller et al., Annu. Rev. Nucl. Part. Sci. **57**, 205 (2007). 15, 16

[15] M. P. McCumber, PHENIX Analysis Notes 646 (2007). 27

[16] M. P. McCumber (PHENIX Collaboration), J. Phys. G **35** 104081 (2008). 28

[17] P. W. Stankus, PHENIX Technical Notes 412 (2005). 29

[18] S. S. Adler et al. (PHENIX Collaboration), Phys. Rev. C **71**, 051902 (2005). 31

[19] D.G. d'Enterria, G. Martinez, L. Aphecetche, H. Delagrange, Y. Schutz, G. David, S. Mioduszewski, PHENIX Analysis Notes 115 (2002). 33

[20] A. Adare et al. (PHENIX Collaboration), Phys. Rev. C **80**, 024908 (2009). 34, 36

[21] S. S. Adler et al. (PHENIX Collaboration), Phys. Rev. Lett **98**, 172302 (2007). 38

[22] S. S. Adler et al. (PHENIX Collaboration), Phys. Rev. D **72**, 072002 (2006). 48

[23] J. Alitti et al. (UA2 Collaboration), Phys. Lett. B **263**, 544 (1991). 50

[24] S. Abachi et al. (D0 Collaboration), Phys. Rev. Lett. **77**, 5011 (1996). 50

[25] B. Abbott et al. (D0 Collaboration), Phys. Rev. Lett. **84**, 2786 (2000). 50

[26] F. Abe et al. (CDF Collaboration), Phys. Rev. Lett. **68**, 2734 (1992). 50

[27] F. Abe et al. (CDF Collaboration), Phys. Rev. D **(**48), 2998 (1993). 50

[28] D. Acosta et al. (CDF Collaboration), Phys. Rev. D **65**, 112003 (2002). 50